AGU ADVANCING EARTH AND SPACE SCIENCE

JGR Solid Earth

RESEARCH ARTICLE
10.1029/2021JB022071

Dilatancy and Compaction of a Rate-and-State Fault in a Poroelastic Medium: Linearized Stability Analysis

Elías Rafn Heimisson[1,2], **John Rudnicki**[3], **and Nadia Lapusta**[1,4]

[1]Seismological Laboratory, California Institute of Technology, Pasadena, CA, USA, [2]Swiss Seismological Service, ETH Zurich, Zurich, Switzerland, [3]Department of Civil and Environmental Engineering and Department of Mechanical Engineering, Northwestern University, Evanston, IL, USA, [4]Department of Mechanical and Civil Engineering, California Institute of Technology, Pasadena, CA, USA

Key Points:

- We analyze stability of a rate-and-state fault in a poroelastic solid with fully coupled dilatancy
- We show that dilatancy stabilization can also occur in a highly diffusive bulk if shear zone permeability is low
- We identify a new stabilizing mechanism associated with the mechanical expansion of the shear zone

Correspondence to:

E. R. Heimisson,
eheimiss@caltech.edu;
elias.heimisson@sed.ethz.ch

Citation:

Heimisson, E. R., Rudnicki, J., & Lapusta, N. (2021). Dilatancy and compaction of a rate-and-state fault in a poroelastic medium: Linearized stability analysis. *Journal of Geophysical Research: Solid Earth*, *126*, e2021JB022071. https://doi.org/10.1029/2021JB022071

Received 17 MAR 2021
Accepted 24 JUN 2021

Abstract Faults in the crust at seismogenic depths are embedded in a fluid-saturated, elastic, porous material. Slip on such faults may induce transient pore pressure changes through dilatancy or compaction of the gouge or host rock. However, the poroelastic nature of the crust and the full coupling of inelastic gouge processes and the host rock have been largely neglected in previous analyses. Here, we present a linearized stability analysis of a rate-and-state fault at steady-state sliding in a fully-coupled poroelastic solid under in-plane and anti-plane sliding. We further account for dilatancy of the shear zone and the associated pore pressure changes in an averaged sense. We derive the continuum equivalent of the analysis by Segall and Rice (1995, https://doi.org/10.1029/95jb02403), and highlight a new parameter regime where dilatancy stabilization can act in a highly diffusive solid. Such stabilization is permitted since the time scale of flux through the shear zone and diffusion into the bulk can be very different. A novel aspect of this study involves analyzing the mechanical expansion of the shear layer causing fault-normal displacements, which we describe by a mass balance of the solid constituent of the gouge. This effect gives rise to a universal stabilization mechanism in both drained and undrained limits. The importance of the mechanism scales with shear-zone thickness and it is significant for wider shear zones exceeding approximately 1 cm. We hypothesize that this stabilization mechanism may alter and delay an ongoing shear localization process.

1. Introduction

Recently, the role of fluids in faults has received great interest for two main reasons: first, by the discovery of a strong causal link between fluid injection and induced seismicity (e.g., Ellsworth, 2013); second, by the mounting evidence that slow slip and tremor are generated at high ambient fluid pressures (e.g., Bürgmann, 2018). A topic of notable recent interest in studies of induced seismicity is the role of poroelasticity. The slow slip and tremor literature has been significantly influenced by the idea of dilatancy and how dilatancy can stabilize fault slip and generate slow slip events. Recently, it has become clear that the topics of slow slip and aseismic transients in nature and human-induced seismicity are closely linked. For example, Bhattacharya and Viesca (2019) and Viesca and Dublanchet (2019) have shown how spontaneous aseismic and slow slip transients arise on faults subject to pore-pressure changes. Torberntsson et al. (2018) investigated slow and fast slip in response to fluid injection near a fault in a poroelastic solid. Further, dilatancy as a stabilizing mechanism for faults subjected to fluid injection has been studied recently (Ciardo & Lecampion, 2019). This study combines both poroelasticity and dilatancy to understand frictional sliding in a fully coupled sense, where pore pressure changes of the shear zone influence the bulk and vice versa. In this introduction, we start by discussing poroelasticity, then we review the concept of dilatancy, and finally we provide an overview of the paper.

Biot's theory of poroelasticity has gained much interest in the study of induced seismicity (Segall & Lu, 2015) because fluid injection does not only change pore pressure, but also induces long-ranging stress interactions through the coupling of fluid pressure and straining of the porous rock. It is well established that the crust behaves as a poroelastic solid (Jónsson et al., 2003) and thus Biot's theory of poroelasticity offers a more realistic way to model the earth's crust than simple elasticity.

The role of poroelasticity in the propagation of shear cracks and frictional sliding has been a subject of interest for decades (Dunham & Rice, 2008; Heimisson et al., 2019; Rice & Cleary, 1976; Rice & Simons, 1976;

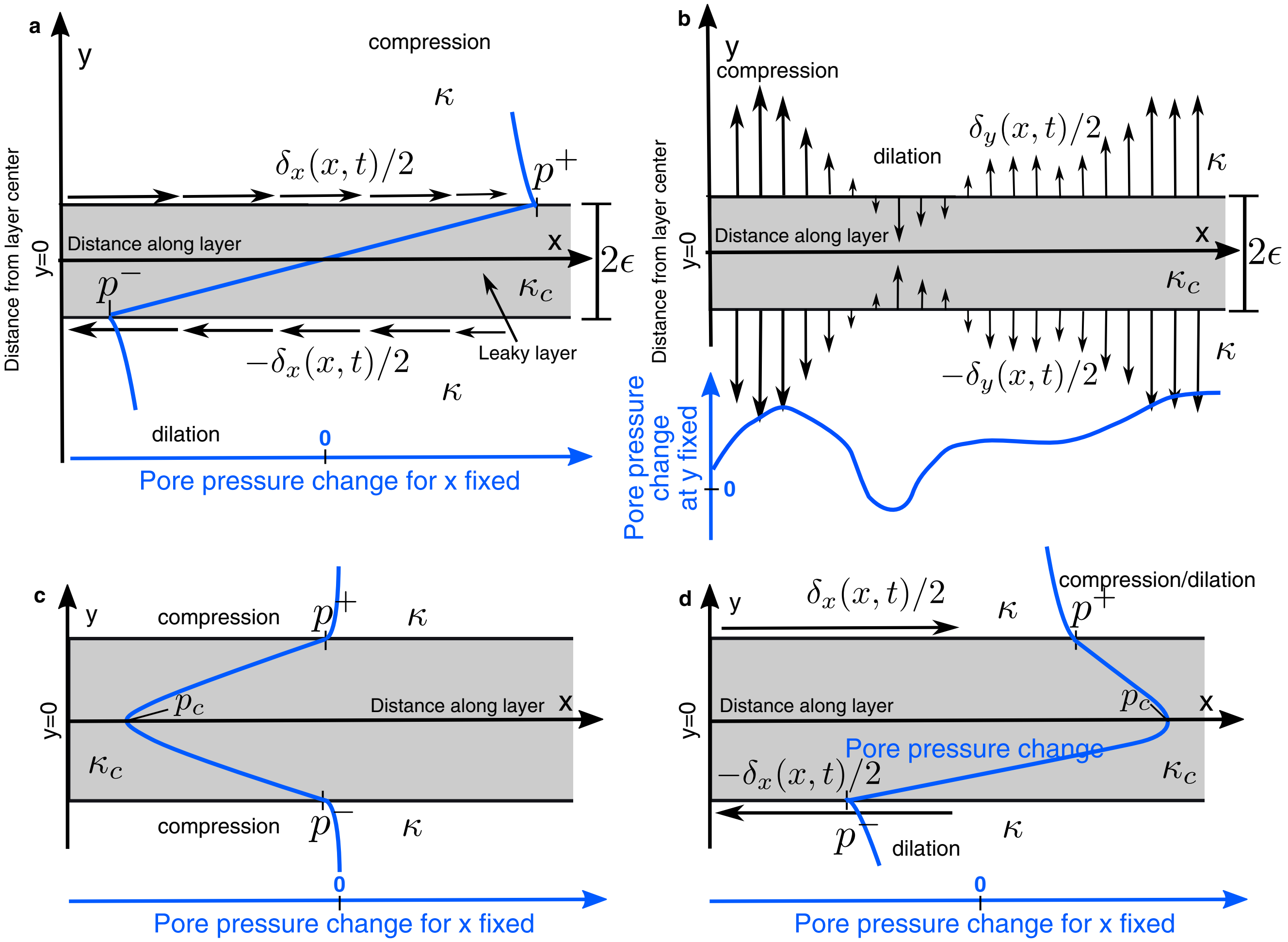

Figure 1. We explore various ways in which the deformation of a leaky and pressurized thin shearing layer of thickness 2ϵ and mobility κ_c, which we consider to be the shear zone, may couple to the surrounding poroelastic medium of mobility κ. (a) In-plane shear across the thin layer (indicated by horizontal arrows) compresses the bulk material on one side of the shear crack tip and dilates the material on the other. Due to poroelastic coupling, this increases pore pressure on the compressive side of the layer and decreases the pore pressure on the dilation side. This case, in which changes from pore pressure arise only from slip $\delta_x(x, t)$, was explored by Heimisson et al. (2019). (b) Processes in the thin layer, such as injection or inelastic dilation/compaction, may cause the layer to contract or expand (as indicated by vertical arrows), which would cause pore pressure changes in the surrounding medium. For example, expansion of the layer (outward facing arrows) would compress the bulk (as indicated by the word "compression") and raise pore pressure in the bulk. (c) Internal pore pressure decrease can occur in the layer, $p_c(x, t) < 0$, perhaps due to inelastic dilation. The flow of pore fluids into the layer from the surrounding medium would cause compression adjacent to the layer in the bulk. (d) An example of a situation that combines changes in the pore pressure $p_c(x, t)$ in the layer (an increase in this case, e.g., due to fluid injection) and bulk effects of shear across the layer. The bulk material adjacent to the fault may undergo both compression and dilation (due to slip) and dilation due to pore pressure flow from the fault to the bulk if pressure $p_c(x, t)$ exceeds the slip induced pressure changes at the boundary, as shown.

Rudnicki & Koutsibelas, 1991; Rudnicki & Rice, 2006). Perhaps the most intriguing aspect of this problem is the role of the pore pressure changes during in-plane, or mode II, sliding. Such sliding induces volumetric stress change on both sides of the fault plane, whereas anti-plane or mode III sliding does not induce volumetric stress. During in-plane sliding, the volumetric stress change is compressive on one side and expansive on the other, with a discontinuity across the plane. This raises an important question of which pore pressure should be used to compute the effective normal stress at the frictional interface. Field observations of faults suggest that the principal slip zone often lies at the boundary of the damage zone and the fault core (F. M. Chester et al., 1993, 2004; Dor et al., 2006). The fault core generally has a much lower permeability than the damage zone (Wibberley & Shimamoto, 2003). In models that idealize the fault core as an impermeable surface, the relevant pore pressure is often taken to be the value at an infinitesimal distance from the shear zone (presented as p^+ or p^- in Figure 1a but no core depicted) (Dunham & Rice, 2008; Heimisson et al., 2019; Rudnicki & Koutsibelas, 1991; Rudnicki & Rice, 2006). Another view was presented by Jha and

Juanes (2014), in which shear localization occurs preferentially in the fault core where effective normal stress is low and thus the relevant pore pressure is where it is highest on either side of the fault core. However, such a model requires the shear localization zone to be able to change sides dynamically in the core depending on how the normal stress evolves. We conclude that significant uncertainty remains regarding how slip-induced pore pressure changes interact with the shear zone and/or fault core and dynamically change the effective normal stress.

Here, we introduce a somewhat conservative and simplified view and select the average pore pressure through the shear zone as the relevant pore pressure for computing the effective normal stress. We allow the shear zone to have a different permeability than the host rock. This choice of the relevant pore pressure implies that the shear-zone width is initially at steady state and not localizing or delocalizing at any relevant frictional or diffusional time scale. As we explain in more detail in the next section, the problem of selecting the appropriate pore pressure for shear of a finite-width fault zone in a poroelastic medium remains largely unsolved and likely needs explicit modeling.

When sheared and perturbed, for example, due to changes in slip speed, the fault gouge can dilate or compact. The process changes the void volume fraction of the gouge, which is also approximately the porosity of the gouge. If the volume change occurs faster than the fluid pressure can equilibrate, then the changes in the void volume fraction can dramatically alter the pore pressure. Much like other processes of frictional interfaces, the influence of these volume changes on frictional strength has not been derived from first principles. The related models and theory have been largely derived and developed based on empirical observations (e.g., Lockner & Byerlee, 1994; Marone et al., 1990; Proctor et al., 2020). Nevertheless, the process can be understood as the result of continuous rearranging and deformation of grains in the gouge to accommodate sliding. Based on experimental results (Marone et al., 1990), Segall and Rice (1995) postulated, following the critical state concept in soil mechanics, the existence of a steady-state void volume (or porosity) which establishes itself eventually for sliding at steady state with a given constant slip velocity. If the slip speed increases or decreases, the granular structure dilates or compacts, respectively. Dilatancy and compaction are well established from laboratory frictional experiments spanning three decades (e.g., Lockner & Byerlee, 1994; Marone et al., 1990; Proctor et al., 2020) and have been attributed to strain-rate hardening of visco-plastic asperity contacts in simulations of rough interfaces (Hulikal et al., 2018) as well as the dynamics of grains in simulations of granular media without viscoplasticity (Ferdowsi & Rubin, 2020). In addition to being induced by shear of granular materials, dilatancy is well known to accompany inelastic deformation of brittle rocks (Brace et al., 1966) and can be induced by earthquake nucleation and rupture (Lyakhovsky & Ben-Zion, 2020; Templeton & Rice, 2008). Dilatancy accompanying earthquake nucleation and rupture will likely happen at a different scale than the granular dilatancy and further increase the complexity of pore-pressure changes in the vicinity of the shear-zone (Viesca et al., 2008). In this paper we will not further consider this type of dilatancy.

Segall and Rice (1995) used the laboratory observations of Marone et al. (1990), which documented porosity changes in a velocity-stepping experiment under drained conditions, to propose a model for the observed porosity changes. They postulated the existence of a steady-state porosity which depends on the slip velocity and to which the porosity evolves with slip:

$$\dot{\phi} = -\frac{V}{L}\left(\phi - \phi_0 - \gamma \log\left(\frac{V}{V_0}\right)\right), \tag{1}$$

where ϕ_0 is the steady-state porosity at the reference slip speed V_0, L is the characteristic state evolution distance, and γ is an empirical dilatancy coefficient. Segall and Rice (1995) also proposed a related dilatancy model in which the porosity depends on the frictional state variable that reflects the evolution of the sliding surface(here Equation 33). Near steady-state sliding, the two models behave the same, but some differences occur away from the steady state. Recent experiments have suggested that a state-variable formulation may be more appropriate (Proctor et al., 2020). We emphasize that even though γ is referred to as a dilatancy coefficient, the formulations by Segall and Rice (1995) describe both dilatancy and compaction, or alternatively void volume changes.

Segall and Rice (1995) then coupled the dilatancy model with a simple single-degree-of-freedom spring slider system and a membrane diffusion model (Rudnicki & Chen, 1988) and carried out a linearized stability analysis and numerical simulations. This work was revisited by Segall et al. (2010) who expanded previous work on the spring-slider stability analysis and explored a more elaborate homogenous diffusion model. However, the main goal of Segall et al. (2010) was to explore dilatancy as a mechanism that can quench earthquake instability and generate slow slip. Models using dilatancy for stabilization have found agreement with observed behavior of subduction zone slow-slip events (e.g., Dal Zilio et al., 2020; Liu, 2013; Segall et al., 2010). These models go beyond the spring-slider analysis and explore a rate-and-state fault with dilatancy coupled to an elastic continuum. However, to date, dilatancy coupled to a poroelastic bulk, as we do here, has not been explored.

In this study, we formulate a closed system of equations and carry out a linearized stability analysis of a rate-and-state fault with dilatancy coupled to a poroelastic bulk. Further, we allow the shear zone to have different diffusivity from the bulk.

The paper starts by discussing the governing equations, boundary conditions, and various effects that may arise from frictional sliding and dilatancy or compaction in a poroelastic solid. That section concludes by presenting solutions for stresses and pore pressures at the fault in a joint Fourier-Laplace transform domain. The following section derives various constitutive relationship for the shear layers and presents the rate-and-state friction law. The section concludes with the mathematical formulation of the linearized stability analysis. Finally, we present the results and derive several simple approximations that characterize stability in certain limiting cases. The section concludes by comparing these approximations to the full solutions to the characteristic equation obtained through a standard root-finding algorithm.

2. Problem Statement and Boundary Conditions

We consider two poroelastic half spaces with interface at $y = 0$ that are uniformly sliding past each other with slip rate V_0 across the interface which is spatially and temporally uniform. V_0 is small enough such that inertial effects and wave-mediated stress transfer can be ignored. The interface is at a uniform shear stress τ_0 and effective normal stress σ_0 and thus friction coefficient $f_0 = \tau_0/\sigma_0$. The pore pressure p is also at equilibrium and spatially uniform. At time $t = 0$, this steady-state configuration is perturbed by introducing a Fourier mode slip perturbation $\delta_x = e^{st+ikx}$, with the total slip for $t > 0$ being $V_0 t + \delta_x$. This non-uniform (or heterogeneous) slip excites spatial variation in slip speed, shear stress, pore-pressure, and normal stress.

The displacements u_i and pressure changes p relative to an equilibrium pressure state are governed four coupled partial differential equations. These are (e.g., Detournay & Cheng, 1995)

$$Gu_{i,kk} + \frac{G}{1-2\nu}u_{k,ki} = \alpha p_{,i} \tag{2}$$

and

$$\frac{1}{M}p_{,t} - \kappa p_{,kk} = -\alpha u_{k,kt}, \tag{3}$$

where u_i are displacements and we have assumed that body forces are negligible. The equations are presented in the index notation. Subscript "$, t$" indicates the partial derivative with respect to time, subscript "$, i$" indicates the partial derivative with respect to the spatial coordinate i. Index $i = 1$ refers to the x axis, which lies in the fault plane. Index $i = 2$ refers to the y axis that is, perpendicular to the fault plane. Finally, index $i = 3$ corresponds to the z axis, but all fields will be assumed invariant in that direction since we will conduct a plane-strain analysis. Repeated indices such as "kk" represent sum over all spatial indices. Finally, the material parameters are denoted as follows, G: shear modulus, ν: drained Poisson's ratio, α: Biot-Willis parameter, M: Biot modulus. Finally, κ is the mobility, which is defined as the ratio between the permeability and fluid viscosity. Later we shall replace some of these parameters with other poroelastic parameters for more compact and intuitive expressions. In Appendix A, we provide expressions for converting between poroelastic parameters and Table A1 with important fixed parameters.

Under the assumption of the plane strain, the four coupled equations above can be decoupled and written out in terms of displacement functions $\mathcal{E}$ and $\mathcal{S}$ derived by Verruijt (1971) and McNamee and Gibson (1960), but see also Detournay and Cheng (1995) for a more pedagogical description. We follow the procedure outlined in the appendix of Heimisson et al. (2019), but solve the system of equations for a more general set of boundary conditions:

$$\lim_{y\to 0^{\pm}} u_x^+ - u_x^- = \delta_x, \tag{4}$$

$$\lim_{y\to 0^{\pm}} u_y^+ - u_y^- = \delta_y, \tag{5}$$

$$\lim_{y\to \pm\infty} u_i^{\pm} = 0, \tag{6}$$

$$\lim_{y\to \pm\infty} p^{\pm} = 0, \tag{7}$$

$$\lim_{y\to 0^{\pm}} \sigma_{xy}^+ - \sigma_{xy}^- = 0, \tag{8}$$

$$\lim_{y\to 0^{\pm}} \sigma_{yy}^+ - \sigma_{yy}^- = 0, \tag{9}$$

where + and − superscripts refer to the $y > 0$ and $y < 0$ half-spaces respectively, and σ_{xy}^+, σ_{xy}^-, σ_{yy}^+, and σ_{yy}^- refer to the shear and normal perturbations in stress on top of the initial uniform values. We note that boundary conditions are applied at $y \to 0^{\pm}$, which contains a layer with thickness 2ϵ as shown in Figure 1. We assume that the layer is "thin" and can be treated through the boundary conditions at $y \to 0^{\pm}$. In other words, we require that $\epsilon \ll \lambda_{min}$, where λ_{min} is the smallest length-scale over which any physical fields vary along the x axis. This can be regarded as a boundary layer approach where the outer solution treats the shear zone as a mathematical zero-thickness interface, but the inner solution treats it as having a finite thickness.

The first two boundary conditions describe the deformation of the thin layer by arbitrary shearing, contraction, or expansion of the layer. The displacement discontinuities δ_x and δ_y across the layer are presented as occurring at the boundaries (Figures 1a and 1b). However, as long as the layer is thin, these displacements could be internal to the layer. For example, $\delta_x(x, t)$ could both represent an infinitesimally thin slip surface within the layer (e.g., Heimisson et al., 2019), or it could represent a distributed shear throughout the layer.

The third and fourth boundary conditions guarantee that the displacements and pressure changes vanish at $y \to \pm\infty$. The fifth and sixth boundary conditions enforce that shear and normal stress are continuous across the layer. This condition also makes sense only for a thin layer.

Finally, we formulate a boundary condition for the pore pressure at the layer boundary. First, we recognize that this layer may generate pore pressure changes through several processes that may be slip-dependent, such as compaction or dilation (Segall & Rice, 1995), chemical such as dehydration reactions, or simply due to applied perturbations from, for example, injection into the shear layer. Second, we recognize that such interface layers are generally produced by frictional wear, and such alterations may dramatically change the permeability (e.g.,Behnsen & Faulkner, 2011; Caine et al., 1996; Wibberley & Shimamoto, 2003). The difference in pore pressure at the boundary relative to the internal pore pressure determines the direction of the fluid flux. Taking $p_c(x, t)$ to be the pore pressure in the center of the layer (Figures 1c and 1d), we can approximate the pressure gradient on the ± sides of the layer as $(p^{\pm} - p_c)/\epsilon$. We use Darcy's law to provide a flux boundary condition that equates the fluid flux out of each side of the layer to the flux into the bulk:

$$\left.\frac{dp^{\pm}}{dy}\right|_{y=0^{\pm}} = \pm\frac{\kappa_c}{\kappa}\frac{(p^{\pm} - p_c)}{\epsilon}, \tag{10}$$

where $\varkappa_c$ is the mobility within the shear layer. Equation 10 generalizes the leaky plane boundary condition of Song and Rudnicki (2017) and reduces to it if $p_c = 0$. Note that Equation 10 can result in an asymmetric flux out of the layer.

If we assume that Equation 10 holds rigorously, then the pore pressure in the layer can be written as follows:

$$\begin{aligned} p(y) &= \frac{y}{\epsilon}(p^{+} - p_c) + p_c \quad \text{if } 0 < y < \epsilon \\ p(y) &= \frac{y}{\epsilon}(p_c - p^{-}) + p_c \quad \text{if } -\epsilon < y < 0. \end{aligned} \tag{11}$$

2.1. Solutions to Slip and Pore Pressure Changes in Fourier-Laplace Domain: In-Plane Shear

Let us define the joint Fourier-Laplace transform:

$$\bar{\hat{\delta}}_x(s,k) = \int_0^{\infty}\int_{-\infty}^{\infty} \delta_x(t,x)e^{-ikx-st}dxdt, \tag{12}$$

applied here to the slip $\delta_x(x, t)$, or displacement discontinuity across the layer in the x direction, where the bar symbol represents the Laplace transform in time and the hat represents the Fourier transform along the x spatial axis. Some symbols may not carry the hat symbol if they are explicitly written out in terms of wavenumber k.

Following the procedure outlined by Heimisson et al. (2019), we derive solutions for shear stress, pore pressure, and normal stress change at the slip surface ($y \to 0^{\pm}$) in the Fourier-Laplace domain. In the Laplace-Fourier transform domain, we obtain the following relationships between change in shear stress $\bar{\hat{\tau}}'$, pore pressure change on either side of the layer $\bar{\hat{p}}^{\pm}$, and change in total normal stress $\bar{\hat{\sigma}}_{yy}$ in terms of $\bar{\hat{\delta}}_x$, $\bar{\hat{\delta}}_y$, and $\bar{\hat{p}}_c$:

$$\bar{\hat{\tau}}' = -\frac{G\,|\,k\,|\,\bar{\hat{\delta}}_x}{2(1-\nu_u)}\bar{H}_1(s,k) \tag{13}$$

and

$$\bar{\hat{p}}^{\pm} = \mp\frac{ikGB\bar{\hat{\delta}}_x}{3}\frac{1+\nu_u}{1-\nu_u}\bar{H}_2(s,k) - \bar{\hat{p}}_c\frac{\mathcal{F}}{\mathcal{F}+1}\left(\bar{H}_2(s,k)-1\right) + \frac{|\,k\,|\,GB\bar{\hat{\delta}}_y}{3}\frac{1+\nu_u}{1-\nu_u}\bar{H}_2(s,k), \tag{14}$$

and

$$\bar{\hat{\sigma}}_{yy} = \bar{\hat{p}}_c\frac{3}{2B(1+\nu_u)}\frac{\mathcal{F}}{\mathcal{F}+1}(\bar{H}_1(s,k)-1) - \frac{G\,|\,k\,|\,\bar{\hat{\delta}}_y}{2(1-\nu_u)}\bar{H}_1(s,k), \tag{15}$$

where

$$\bar{H}_1(s,k) = 1 - \frac{2(\nu_u-\nu)}{1-\nu}\frac{ck^2}{s}\frac{1+\mathcal{F}}{\mathcal{F}+\sqrt{1+s/ck^2}}\left(\sqrt{1+s/ck^2}-1\right), \tag{16}$$

and

$$\bar{H}_2(s,k) = \frac{\sqrt{1+s/ck^2}-1}{\sqrt{1+s/ck^2}+\mathcal{F}}. \tag{17}$$

$\mathcal{F}$ is a dimensionless group that characterizes the importance of flux across the fault:

$$\mathcal{F} = \frac{\kappa_c}{\kappa} \frac{1}{|k| \epsilon}. \tag{18}$$

2.2. Solutions to Slip and Pore Pressure Changes in Fourier-Laplace Domain: Anti-Plane Shear

Having solved the more complex in-plane shear problem, we may deduce the simpler anti-plane shear case. We note:

1. Any term of Equations 13–15 that is, linear in $\bar{\hat{p}}_c$ and $\bar{\hat{\delta}}_y$ must be unchanged from the in-plane case, since these terms do not depend on fault-parallel slip
2. Any term of Equations 13–15 that is, linear in $\bar{\hat{\delta}}_x$ must be represented by the corresponding elastic anti-plane slip relationship, since anti-plane slip induces no volumetric stress and thus does not induce instantaneous or transient pore pressure response

We thus arrive at the corresponding anti-plane shear relationships. We have:

$$\bar{\hat{\tau}}' = -\frac{G|k|\bar{\hat{\delta}}_x}{2}, \tag{19}$$

as was identified by Rice and Ruina (1983); Rice et al. (2001). Further, we find:

$$\bar{\hat{p}}^{\pm} = -\bar{\hat{p}}_c \frac{\mathcal{F}}{\mathcal{F}+1}\left(\bar{H}_2(s,k) - 1\right) + \frac{|k| GB\bar{\hat{\delta}}_y}{3} \frac{1+\nu_u}{1-\nu_u} \bar{H}_2(s,k) \tag{20}$$

and

$$\bar{\hat{\sigma}}_{yy} = \bar{\hat{p}}_c \frac{3}{2B(1+\nu_u)} \frac{\mathcal{F}}{\mathcal{F}+1} (\bar{H}_1(s,k) - 1) - \frac{G|k|\bar{\hat{\delta}}_y}{2(1-\nu_u)} \bar{H}_1(s,k), \tag{21}$$

where changes in normal stress σ_{yy} are identical to the in-plane case. It may seem surprising that the relationships above for anti-plane shear depend on Poisson's ratios (all except [Equation 19], the slip to shear stress relationship). However, the terms with Poisson's ratio are not stress components that arise from sliding, but rather ones that result from pressurization of the layer and dilation/compaction of the layer. The terms that depend on δ_y represent mode I contribution of the interface deformation and terms with p_c represent contributions from the pressure change at the interface. These contributions do not depend on the primary mode of sliding and are thus the same for the in-plane and anti-plane cases.

3. Constitutive Relations for a Thin Layer

Here we describe the center pore pressure change p_c and the layer-perpendicular displacements δ_y in terms of the slip δ_x.

3.1. Frictional Constitutive Law

First, we consider the force balance within the layer:

$$\frac{\tau(x,t)}{\sigma(x,t) - p(x,y,t)} = f(x,y,t) \quad \text{for} - \epsilon < y < \epsilon, \tag{22}$$

where τ and σ are the shear stress and the effective normal stress in absence of pore pressure perturbations, respectively. Thus $\sigma = \sigma_0 + \sigma_{yy}$, where σ_0 is the total effective normal stress at equilibrium, when there are no perturbations present in stresses or pore-pressure. The effective normal stress at equilibrium (σ_0) is thus the difference between the total ambient equilibrium normal stress and the ambient equilibrium pore-pressure, but these two scalars are always combined in σ_0. We emphasize that perturbations in pore-pressure are not written as a part of σ, while the ambient background pore-pressure is included in σ as a part of σ_0. Similarly $\tau = \tau_0 + \tau'$ where τ_0 is the absolute equilibrium shear stress and τ' represents any perturbations in shear stress from slip, pore-pressure or from external loading. The subscript $_0$ refers to a later assumption where we consider the system to be in equilibrium at $t = 0$ (see Section 3.4).

We assume that τ and σ are constant with respect to y in the layer because the layer is thin. This assumption also implies that inertia can be ignored in the layer (Rice et al., 2014). f describes the frictional resistance at each point in the layer and p is the pore pressure perturbation assumed to follow the linear pressure distribution in Equation 11. In order to obtain the approximate frictional resistance of the entire layer, we average with respect to y using Equation 11:

$$\tau\frac{(p_c - p^+)\log\left(\frac{\sigma - p^-}{\sigma - p_c}\right) + (p_c - p^-)\log\left(\frac{\sigma - p^+}{\sigma - p_c}\right)}{2(p_c - p^-)(p_c - p^+)} = \langle f \rangle, \tag{23}$$

where now all fields depend on x and t (not written explicitly for compactness), but not on y within the layer.

We assume that the layer-averaged fictional resistance is described by the rate-and-state friction law (e.g., Dieterich, 1979; Marone, 1998; Ruina, 1983):

$$\langle f \rangle = \frac{1}{2\epsilon}\int_{-\epsilon}^{\epsilon} f(x,y,t)dy = f_0 + a\log\left(\frac{V}{V_0}\right) + b\log\left(\frac{V_0\theta}{L}\right), \tag{24}$$

where a is a constitutive parameter that weights the rate dependence of friction under constant state (also called the direct effect) and b is a constitutive parameter that weights the state dependence of friction at constant slip rate. V thus represents the slip rate of one side of the shear zone layer relative to the other, or in other words the integrated shear strain rate across the layer. L is the characteristics slip distance over which the state θ evolves. A mathematical definition of θ is offered later in the section where we introduce the state evolution law. In order to maintain consistency with the linearized stability analysis, discussed and presented in Section 3.4, we select the nominal coefficient of friction $f_0 = \tau_0/\sigma_0$ and the nominal slip speed as V_0 as the values at time $t = 0$, and the nominal state $\theta_0 = L/V_0$ as the steady-state value at time $t = 0$.

Equation 22 is non-linear, both in terms of strength dependence on pore-pressure and the coefficient of friction in Equation 24. The linearization of the friction coefficient is addressed in Section 3.4. Here, we present the linearization with respect to small changes in pore pressure, to provide a more intuitive expression than Equation 23. The linearization renders:

$$\tau = \tau_0 + \tau'(t) = (\sigma_0 + \sigma_{yy}(t) - \langle p(t) \rangle)\left[f_0 + a\log\left(\frac{V}{V_0}\right) + b\log\left(\frac{V_0\theta}{L}\right)\right], \tag{25}$$

where the relevant average pore pressure $\langle p \rangle$ in the layer can be written as:

$$\langle p \rangle = \frac{1}{2\epsilon}\int_{-\epsilon}^{\epsilon} p(y)dy = \frac{1}{2}\left(p_c + \frac{p^+ + p^-}{2}\right). \tag{26}$$

Hence we conclude that, given our assumptions, we can simply use the average pressure in the layer as the relevant pore pressure in computing the effective normal stress in computing the shear resistance. As a reminder, our assumptions include the linear pore pressure distribution within the shear layer, the averaging of frictional strength described earlier in this section, and considering changes in pore pressure that are small compared to σ.

We note that the average pore pressure in the (distributed) shearing layer that we use in this study may not be a universally valid approach. In the presence of a thin low-permeability structure surrounding or next to the shearing layer, as typical for a fault core, the relevant pore pressure may be different (Heimisson et al., 2019; Jha & Juanes, 2014). Such structures are expected to be significant in well-developed fault zones (Caine et al., 1996). Our view could be most appropriate for less developed faults and laboratory settings where the shear zone represents simulated gouge, or scenarios where the fault core may not generate a significant permeability contrast or flow barrier with the shear zone and/or the surrounding rock.

Furthermore, the localization of slip in fluid-saturated thin granular layers of distributed shear is not fully understood at present and may require explicit modeling. If an ongoing localization process occurs, we also expect the relevant pore pressure to evolve in a complex way that requires explicit modeling. For example, studies indicate that, as instability develops, a localization process occurs and a distributed shear layer may collapse to a much narrower slip "surface" with the width of the order of several microns (Platt et al., 2014; Rice et al., 2014). We expect that the relevant effective normal stress for shear resistance would then be determined by the pore pressure over that localized shear surface.

Equation 25 requires an equation for the evolution of the state variable θ, for example, the aging law:

$$\frac{d\theta}{dt} = 1 - \frac{\theta V}{L} - \frac{\alpha_{LD}\theta}{b\sigma}\dot{\sigma} \tag{27}$$

or the slip law (Ruina, 1983) These state evolution laws are identical when linearized around steady state slip and our analysis encompasses both (see Section 3.4). Here, we have included the correction of Linker and Dieterich (1992) for the dependence of state on normal stress. This dependence is proportional to the empirical Linker and Dieterich (1992) constant α_{LD}, which is typically between 0 and 0.5, but always less than f_0.

3.2. Constitutive Equations for Pore Pressure in the Layer

Now we derive an evolution equation for the average pore pressure in the layer. Following Segall and Rice (1995), the fluid mass conservation in the layer requires:

$$\frac{\partial m}{\partial t} + \frac{\partial q}{\partial y} = 0, \tag{28}$$

where m is the fluid mass content and q is the fluid mass flux. This expression considers the fluid mass flux along the layer (along x) to be negligible, which is valid if flux along y dominates over flux along x. One obvious example is if the mobility or permeability in y direction is much larger than in the x direction. However, we expect this to hold more generally since the flux along y is proportional to $1/\epsilon$ but the flux along x is proportional to k and $\epsilon k \ll 1 \Rightarrow k \ll 1/\epsilon$. Nevertheless, this also depends on the relation between the permeability of the host rock and permeability of the shear layer. If the host-rock is impermeable (or has low permeability compared to the one along the shear layer) then the flux along x cannot be ignored. The assumption that shear zone flux only occurs in fault normal direction is commonly applied in studies of thermal pressurization (e.g., Bizzarri & Cocco, 2006; Rice, 2006).

We write $m = \rho_f n$, where ρ_f is the fluid density and $n = n^e + n^p$ is the sum of the elastic and plastic void volumes. Taking the time derivative of m yields

$$\dot{m} = \dot{\rho}_f n + \rho_f \dot{n}. \tag{29}$$

We now propose linearized relationships for the elastic void compressibility $\dot{n}^e = \phi(\beta_n^p \dot{p} - \beta_n^\sigma \dot{\sigma})$ and $\dot{\rho}_f = \rho_{fo}(\beta_f^p \dot{p} + \beta_f^\sigma \dot{\sigma})$, where β_f^p and β_n^p are fluid and elastic void compressibilities, respectively. Superscript p on β_f^p or β_n^p refers to "pressure" and specifies that this compressibility is defined under isotropic volumetric stress or pressure. Superscript σ on β_f^σ or β_n^σ refers to normal stress, specifically here σ_{yy}, and specifies that this compressibility is defined under uniaxial compressive or tensile stress. For example, for a linear elastic solid, $\beta^p = 1/K$, where K is the bulk modulus. However $\beta^\sigma = (1 + \nu)/(3\,K(1 - \nu))$, which is the so called P-wave modulus. For $\nu = 0.25$, we find $\beta^\sigma = 5\beta^p/9$. We assume that $\sigma > 0$ reflects increased compression, or the compression positive convention. Thus increased normal stress reduces the void-volume and decreases the fluid mass in each control volume. We refer the reader to Cocco and Rice (2002) for the detailed discussion of isotropic and uniaxial compressibilities in a poroelastic solid. The reference compressibilities are defined at the reference void fraction ϕ, which we interpret as porosity, and reference fluid density ρ_{fo}. Further, we assume that the plastic void fraction is equal to the plastic porosity: $n^{pl} = \phi^{pl}$, where the superscript "*pl*" refers to "plastic." Thus, we arrive at:

$$\dot{m} = \rho_{fo}\phi(\beta_f^p\dot{p} + \beta_f^\sigma\dot{\sigma}) + \rho_{fo}\phi(\beta_n^p\dot{p} - \beta_n^\sigma\dot{\sigma} + \dot{\phi}^{pl} / \phi). \tag{30}$$

Combining Equations 28 and 30 and integrating over the shear layer yields:

$$2\epsilon\rho_{fo}\phi\Big[(\beta_f^p + \beta_n^p)\langle\dot{p}\rangle + (\beta_f^\sigma - \beta_n^\sigma)\dot{\sigma} + \langle\dot{\phi}\rangle^{pl} / \phi\Big)\Big] + q^+ - q^- = 0, \tag{31}$$

Inserting the expressions for the fluid mass flux given a linear pressure distribution (Equations 10 and 11) provides:

$$\langle\dot{p}\rangle + \frac{\beta_f^\sigma - \beta_n^\sigma}{\beta_f^p + \beta_n^p}\dot{\sigma} = -\frac{\langle\dot{\phi}\rangle^{pl}}{\phi(\beta_f^p + \beta_n^p)} + \frac{\kappa_c}{\epsilon^2\phi(\beta_f^p + \beta_n^p)}\Big(\frac{1}{2}(p^+ + p^-) - p_c\Big). \tag{32}$$

We have thus arrived at an evolution equation that relates normal stress (uniform over the layer) with average pore pressure and dilatancy, where the source of pore pressure stems from inelastic changes in porosity ϕ^{pl}. Segall and Rice (1995) and Segall et al. (2010) proposed that the inelastic porosity is a function of the state $\phi^{pl}(\theta)$. This idea has been further observationally supported by Proctor et al. (2020). We assume that the state variable description of the plastic porosity changes reflects the average porosity change in the shear layer:

$$\langle\phi\rangle^{pl} = \langle\phi_0\rangle^{pl} - \gamma\log\left(\frac{V_0\theta}{L}\right), \tag{33}$$

where γ is a dilatancy coefficient usually taken as $\gamma \sim 10^{-4}$. The rate of change of the inelastic porosity is then given by:

$$\langle\dot{\phi}\rangle^{pl} = -\frac{\gamma}{\theta}\dot{\theta}. \tag{34}$$

It may be useful to summarize, at this stage, the treatment of porosity in the study. If the fault is loaded at rate V_0 and is also slipping at steady state everywhere at V_0, which is a fundamental assumption of the stability analysis, then the porosity is simply ϕ that is, the reference porosity. This means that here the initial value of the plastic porosity in Equation 33 is $\langle\phi_0\rangle^{pl} = 0$. The total porosity is then $\phi + \phi(\beta_n^p p - \beta_n^\sigma\sigma) + \langle\phi\rangle^{pl}$, where the second term is the elastic changes in porosity. We note that often Equation 33 is written to describe the sum of reference porosity plus plastic porosity (e.g., Segall & Rice, 1995; Segall et al., 2010), which can be obtained by replacing $\langle\phi_0\rangle^{pl} = \phi_0$. However, here we have for completeness introduced a separate value for the initial plastic porosity since in general the reference porosity may not be defined as the intial porosity, which may include a plastic porosity change.

3.3. Fault-Normal Displacements of the Shear Layer

We now seek a relationship that describes fault normal expansion or contraction of a thin gouge layer $\delta_y = u_y(y = \epsilon) - u_y(y = -\epsilon)$. We start by stating the conservation of gouge mass, m_g, per unit volume:

$$\frac{\partial m_g}{\partial t} + \frac{\partial}{\partial y}\Big((1-n)\rho_g\dot{u}_y\Big) + \frac{\partial}{\partial x}\Big((1-n)\rho_g\dot{u}_x\Big) = 0, \tag{35}$$

where ρ_g is the gouge density; note that this is not the bulk density but the density of non-porous and intact gouge mass, that is, the solid constituent of the gouge with all pores removed. Deformation u_x and u_y here refer to the internal deformation field of the gouge. Unlike the deformation of the bulk, in the gouge u_x and u_y are representing large strain and non-elastic deformation. Here we have included the $\partial/\partial x$ term for completeness, but we will neglect assuming symmetry across the shear zone, as is discussed later. Now $m_g = (1-n)\rho_g$ and thus:

$$\dot{m}_g = -\rho_g \dot{n} + (1-n)\dot{\rho}_g. \tag{36}$$

following the same arguments as in the previous section, we arrive at a linearized relationship:

$$\dot{m}_g \approx -\rho_{go}\phi\left(\beta_n^p \dot{p} - \beta_n^\sigma \dot{\sigma} + \dot{\phi}^{pl} / \phi\right) + (1-\phi)\rho_{go}\left(\beta_g^p \dot{p} + \beta_g^\sigma \dot{\sigma}\right), \tag{37}$$

where now β_g is the compressibility of the intact and non-porous gouge material and again superscript p and σ refer to the isotropic and uniaxial compressibilities, respectively.

Inserting Equation 37 into Equation 35 and integrating over the shear layer provides a relationship between dilatancy, pressure, and normal stress changes and gouge fault normal displacements:

$$\dot{\delta}_y = 2\epsilon\left(\frac{\phi}{1-\phi}\beta_n^p - \beta_g^p\right)\left[\langle\dot{p}\rangle - \frac{\left(\frac{\phi}{1-\phi}\beta_n^\sigma + \beta_g^\sigma\right)}{\left(\frac{\phi}{1-\phi}\beta_n^p - \beta_g^p\right)}\dot{\sigma}\right] + 2\epsilon\frac{\langle\dot{\phi}\rangle^{pl}}{1-\phi}. \tag{38}$$

If we assume that, at time $t = 0$, the fault is in a pressure equilibrium and sliding at steady state, the equation can be integrated trivially:

$$\delta_y = 2\epsilon\left(\frac{\phi}{1-\phi}\beta_n^p - \beta_g^p\right)\left[\langle p\rangle - \frac{\left(\frac{\phi}{1-\phi}\beta_n^\sigma + \beta_g^\sigma\right)}{\left(\frac{\phi}{1-\phi}\beta_n^p - \beta_g^p\right)}\sigma\right] + 2\epsilon\frac{\langle\phi\rangle^{pl}}{1-\phi}. \tag{39}$$

Where we have assumed that the average of $\dot{u}_x$ with respect to y over the layer thickness is zero such that the x flux term in Equation 35 is essentially neglected. This may be justified by assuming that internal deformation of the shear layer with respect to $y = 0$ is anti-symmetric. This is likely if one side of the fault slips the same amount as the other, which is usually the case for symmetric geometries. We entrust the analysis of what might occur if such symmetry is not present to future work.

3.4. Linearized Stability Analysis

We now seek to analyze the stability of the steady shear (or sliding) in the layer to small perturbations. If the perturbation is small, the friction law and other constitutive relationship can be linearized around the initial steady-state configuration. We seek a solution to the linearized form (Rice et al., 2001) of the friction law and state evolution (Equations 25 and 27, respectively) as well as the linearized equation describing the time-evolution of the layer pressure p_c (Equation 32). We carry out the stability analysis in the joint Laplace-Fourier transform domain (Equation 12), which is equivalent to seeking a solution to the linearized system of equation for a slip perturbation $\delta_x = e^{st+ikx}$, which is applied at $t = 0$ (e.g., Rice et al., 2001).

The goal of the linearized stability analysis is to obtain the characteristic equation where we can solve for s as a function of $k = 2\pi/\lambda$, where λ is wavelength, and other parameters. If the solution has $\Re(s(k)) > 0$, then the steady-state sliding is linearly unstable to the perturbations with corresponding wavenumbers, whereas if $\Re(s(k)) < 0$, the sliding is stable and the perturbations decay exponentially. If $\Re(s(k)) = 0$ perturbations neither grow nor decay; in this case we refer to k as the critical wavenumber k_{cr}, which thus defines a length-scale at which development of instabilities is possible. This important wavenumber is discussed in more detail in Section 4.

We note that the sign of k when it refers to a Fourier-mode perturbation in slip applied to the fault simply reflects the direction of the slip wave as it travels along the interface. The symmetry of the problem indicates that there is no inherent dependence on the wave directionality. Indeed, the term with the opposite sign in p^+ and p^- (Equation 14), which implies the directionality dependence (as was discussed by Heimisson et al. (2019)), cancels when computing $\langle p \rangle$.

Stability analysis of frictional sliding is more commonly done, and perhaps more widely known, in the context of simpler system where this bulk response is neglected. That is, a single degree-of-freedom system commonly referred to as the spring-block slider (e.g., Ruina, 1983; Segall & Rice, 1995; Segall et al., 2010). In this case, the goal is to derive a critical stiffness of the spring, defined as stress drop per unit slip. The spring stiffness is also commonly represented by the symbol k, but here we shall denote it as $\mathcal{K}$ and thus the critical spring stiffness as $\mathcal{K}_{cr}$. If $\mathcal{K} > \mathcal{K}_{cr}$ then instabilities do not develop at steady-state sliding, but if $\mathcal{K} < \mathcal{K}_{cr}$ instabilities can be generated from small perturbations at steady state. In applying the spring-slider analysis to fault stability, which are not uniform in space, the argument is made that the spring stiffness represents a crack stiffness in an elastic medium and the spring stiffness can be replaced with the scaling $\mathcal{K}_{cr} \sim G / L_{cr}$, with L_{cr} being a critical crack length, or half crack length. For quasi-static elastic medium this substitution provides the correct scaling such that $k_{cr} = 2\pi/\lambda_{cr} \sim 1/L_{cr}$ with the only difference being an order 1 constant factor (Rice et al., 2001). However, if transient bulk response, which depends on the wavenumber, plays a role in the stability, such as in an elastodynamic solid (Rice et al., 2001), or poroelasticity (see Heimisson et al. (2019) and this study) this simple correspondence between spring-slider and continuum bulk analysis does not hold anymore in a general sense.

The linearized form of Equations 25 and 27 around steady state sliding can be expressed (Rice et al., 2001):

$$\frac{\mathrm{d}}{\mathrm{d}t}\tau'(t) = \frac{a\sigma_0}{V_0}\frac{\mathrm{d}V}{\mathrm{d}t} + (f_0 - \alpha_{LD})\frac{\mathrm{d}}{\mathrm{d}t}(\sigma_{yy} + p) - \frac{V_0}{L}\left[\tau_0 + \tau'(t) - f_0(\sigma_0 - \sigma_{yy} - p) - \frac{(a-b)\sigma_0}{V_0}(V - V_0)\right], \quad (40)$$

Transforming in the Laplace-Fourier domain renders (Heimisson et al., 2019):

$$\left(s + \frac{V_0}{L}\right)\overline{\hat{\tau}'} = \left[f_0\left(s + \frac{V_0}{L}\right) - \alpha_{LD}s\right](\overline{\hat{\sigma}}_{yy} + \overline{\hat{p}}) + \left[\frac{a\sigma_0}{V_0}s^2 + \frac{(a-b)\sigma_0}{L}s\right]\overline{\hat{\delta}}_x. \quad (41)$$

Expressions for $\overline{\hat{\tau}'}$ and $\overline{\hat{\sigma}}_{yy}$ are provided in Equations 13 and 15, but we note the introduction of the minus sign in front of $\overline{\hat{\sigma}}_{yy}$ due to a change in sign convention since the equation describing friction considers tensile stress to be negative. As previously discussed, the value chosen for the relevant pore pressure within the layer is open to some interpretation but here we take the average value as in Equation 26.

Now we seek to eliminate the eigenfunction $\overline{\hat{\delta}}_x$ from the equation above and retrieve the characteristic equation. However, we first need to derive linear relationships such that $\overline{\hat{p}}_c \propto \overline{\hat{\delta}}_x$ and $\overline{\hat{\delta}}_y \propto \overline{\hat{\delta}}_x$.

Let $\langle \phi^{pl} \rangle = \phi_0 + \Delta\phi_p$, $\theta = L/V_0 + \Delta\theta$, and $V = V_0 + \Delta V$ where Δ indicates a small perturbation around the steady state value, with the latter being the first term on the right hand side of each equation. Inserting into Equation 34 and carrying out a linearization around steady state provides the following expression for $\Delta\dot{\phi}^{pl}$ and the corresponding Laplace transform

$$\Delta\dot{\phi}^{pl} = -\frac{\gamma V_0}{L}\Delta\dot{\theta} \Rightarrow \mathcal{L}(\Delta\dot{\phi}^{pl}) = \overline{\Delta\dot{\phi}}^{pl} = -\frac{\gamma V_0 s}{L}\overline{\Delta\theta}. \quad (42)$$

From Segall and Rice (1995), we have a linearized state evolution law (see also Ruina, 1983):

$$\Delta\dot{\theta} = -\frac{V_0}{L}\Delta\theta - \frac{\Delta V}{V_0} \quad (43)$$

and the Laplace transform renders

$$\overline{\Delta\theta} = -\frac{s\overline{\delta}_x}{V_0\left(s + \frac{V_0}{L}\right)}. \quad (44)$$

Thus the linear relationship between plastic changes in porosity (or alternatively inelastic dilatancy or compaction) is

$$\overline{\Delta\phi}^{pl} = \frac{\gamma}{L}\frac{s\bar{\delta}_x}{\left(s+\frac{V_0}{L}\right)}, \tag{45}$$

where we interpret the relationship as the average representing the plastic changes in porosity within the shear zone.

Applying the Laplace transform to Equation 32 and substituting Equation 45 yields

$$\langle \bar{p}\rangle = \frac{1}{2}\left(\bar{p}_c + \frac{\bar{p}^+ + \bar{p}^-}{2}\right) = -\frac{\gamma}{\beta L}\frac{s}{s+\frac{V_0}{L}}\bar{\delta}_x + \frac{\kappa_c}{2\beta\epsilon^2 s}\left(\bar{p}^+ - 2\bar{p}_c + \bar{p}^-\right), \tag{46}$$

Further substitution of Equation 14 then provides one linear relationship between $\bar{p}_c$, $\bar{\delta}_y$, and $\bar{\delta}_x$. However, another constitutive relationship is needed to eliminate both $\bar{p}_c$ and $\bar{\delta}_y$. This relationship comes from Equation 39 by taking the Laplace transform and substituting Equation 45:

$$\bar{\delta}_y = 2\epsilon\left(\frac{\phi}{1-\phi}\beta_n^p - \beta_g^p\right)\left[\frac{1}{2}\left(\bar{p}_c + \frac{\bar{p}^+ + \bar{p}^-}{2}\right) - \frac{\left(\frac{\phi}{1-\phi}\beta_n^\sigma + \beta_g^\sigma\right)}{\left(\frac{\phi}{1-\phi}\beta_n^p - \beta_g^p\right)}\bar{\sigma}_{yy}\right] + \frac{2\epsilon}{1-\phi}\frac{\gamma}{L}\frac{s\bar{\delta}_x}{\left(s+\frac{V_0}{L}\right)}. \tag{47}$$

Then through substitution of Equations 14 and 15 for the in-plane case, or Equations 20 and 21 for the anti-plane case, we obtain another linear relationship between $\bar{p}_c$, $\bar{\delta}_y$, and $\bar{\delta}_x$.

This means that the linear relationship between stress or pore pressure and $\bar{p}_c$, $\bar{\delta}_y$, and $\bar{\delta}_x$ in Equations 13–15 for in-plane, or Equations 19–21 for anti-plane can all be expressed only in terms of $\bar{\delta}_x$. Then substitutions of those expressions into the characteristic Equation 41 allows for elimination of $\bar{\delta}_x$ and provides finally two equations that can be solved numerically for $s(k)$. The two equations are obtained by requiring that both the real part and imaginary part of the characteristic equation are zero (e.g., Heimisson et al., 2019; Rice et al., 2001). We do not present here the full characteristic equation due to the complexity of the expression but provide a MATLAB code where it is implemented and can be solved (see Acknowledgments). Numerical exploration of the characteristic equation would suggest no more than two roots (within numerical precision). These roots have the same real part and imaginary part except the latter changing sign. However, due to the presence of half-integer terms and the sheer size of the expression, determining analytically the number of roots has not been feasible. In the next section, we discuss some approximation and implications as well as show numerical solutions.

4. Time Scales and Approximations to the Critical Wavenumber

Let us present the results on the stability of steady-state sliding of a dilating shear layer embedded into and coupled with a poroelastic solid. Much of this discussion focuses either on approximate expressions for the critical wavenumber, or solving the characteristic equation numerically using a standard root finding algorithm.

The critical wavenumber $k_{cr} = 2\pi/\lambda_{cr}$ represents the wavenumber at the boundary between stable and unstable sliding. The critical wavenumber marks the point of a Hopf bifurcation where $\mathrm{Re}(s(k_{cr})) = 0$ but $\mathrm{Im}(s(k_{cr})) \neq 0$ in general. A small-magnitude perturbation in slip with a larger wavenumber ($k > k_{cr}$), or alternatively a smaller wavelength, would decay exponentially. However, a perturbation in slip of a smaller wavenumber than k_{cr} ($k < k_{cr}$), or alternatively larger wavelength, would grow and may nucleate a seismic event. A Fourier-mode perturbation with exactly $k = k_{cr}$ would simply oscillate with a fixed frequency and neither grow nor decay.

In the following sections, we present approximations to the critical wavenumber in certain limiting cases. To obtain these approximate expressions, we carry out following steps.

1. We introduce s' and k', which are non-dimensional versions of s and k and are obtained by substitution $s = s'V_0/L$ and $k = k'k_{cr}^{anti}$, where $k_{cr}^{anti} = 2\sigma_0(b-a)/(GL)$ is the critical wavenumber for quasi-static, anti-plane sliding between two elastic solids (Rice et al., 2001). This quantity is of the same order as the corresponding in-plane sliding wavenumber (Rice et al., 2001) but does not depend on Poisson's ratio, which can be either drained or undrained. This non-dimensionalization implies that s' and k' are generally of order unity near critical stability.
2. We introduce a non-dimensional half-thickness ϵ' of the shear layer, by substitution $\epsilon = \epsilon' / k_{cr}^{anti}$. Since a fundamental assumption of the analysis is that $k\epsilon \ll 1$, we may use ϵ' as a small parameter in which the characteristic equation can be expanded.
3. We carry out a Taylor expansion of both the real and imaginary parts of the characteristic equation. We retain terms up to first order in ϵ'. We also explore the leading-order terms that are proportional to $1/\kappa_c$ if appropriate. These terms are retained because they become large if κ_c is small and thus may provide insight into transitional regimes at low shear-zone mobility.

4.1. Characteristic Time Scales

In order to obtain insight into the role of diffusion in the stability of the frictional interface, we start by analyzing the time scales involved as perturbations grow around steady state sliding. The problem has three characteristic time scales. First, a frictional nucleation time scale:

$$t_{nu} = \frac{L}{V_0}, \tag{48}$$

which is a natural time-scale for the evolution of the frictional state and scales how fast instabilities nucleate or decay back to steady state sliding in a stable regime. Further, it offers a first-order approximation to the instability time of sources above steady state in the spring-slider analysis (Heimisson & Segall, 2018).

Second, we investigate the time scale of diffusion into the bulk:

$$t_b = \frac{1}{ck^2}. \tag{49}$$

Lastly, a time scale of flux in the shear layer:

$$t_f = \frac{1}{\mathcal{F}^2 ck^2} = \frac{\kappa^2\epsilon^2}{\kappa_c^2 c} = \frac{c\epsilon^2}{M^2\kappa_c^2}, \tag{50}$$

where the last equality is obtained by the substitution $\kappa = c/M$, which is the relationship between the mobility and hydraulic diffusivity in a linear poroelastic bulk.

From these time scales, we identify two non-dimensional time scales. First,

$$\mathcal{T}_f = \frac{t_{nu}}{t_f} = \frac{LM^2\kappa_c^2}{V_0 c\epsilon^2}, \tag{51}$$

where $\mathcal{T}_f$ represents the ratio of the time scale of nucleation to the time scale of flux through the shear layer. If $\mathcal{T}_f$ is small compared to unity, then nucleation occurs much faster than the fluid flux in the shear layer. Since such flux is needed to minimize the effects of dilational stabilization, we expect that a small value of $\mathcal{T}_f$ corresponds to the limit where dilatancy is important. On the other hand, if $\mathcal{T}_f$ is large, then nucleation occurs over a longer time than the flux and dilatancy can be ignored.

The second non-dimensional time scale is $t_{nu}/t_b = Lck^2/V_0$, however, we substitute $k \rightarrow k_{cr}^{anti}$ since it is not convenient to express the non-dimensional time scale explicitly in terms of k, which is treated as a variable in the characteristic equation. We thus obtain a non-dimensional time scale independent of k:

$$\mathcal{T}_b = \frac{4c\sigma_0^2(b-a)^2}{V_0 G^2 L}, \tag{52}$$

which is valid as long as the critical wavenumber is of the same order as k_{cr}^{anti}. When $\mathcal{T}_b$ is small compared to unity we may effectively ignore the fluid diffusion in the bulk on the time scale of nucleation and we expect undrained bulk response. However, if $\mathcal{T}_b$ is large then fluid in the bulk can diffuse at the time scale of nucleation and the bulk response is drained. For $\mathcal{T}_b \sim 1$, we expect transient poroelastic response of the bulk.

The two non-dimensional time scales here share several parameters, notably the hydraulic diffusivity of the host rock c. Moving forward, we shall investigate different limits of stability by systematically changing either $\mathcal{T}_f$ or $\mathcal{T}_b$ while keeping the other parameter constant.

4.2. Limit of $\kappa_c \rightarrow 0$

Let us analyze a simple limit where the permeability or mobility of the shear layer is zero, in addition to assuming that the bulk response is either drained or undrained. In this limit, as $\epsilon \rightarrow 0$, one can show, for in-plane sliding, that:

$$\left|k_{cr}\right| \simeq k_{cr}^{un}\left(1 - \frac{f_0\gamma}{\beta\sigma_0(b-a)} + \mathcal{O}(\epsilon)\right), \tag{53}$$

where

$$k_{cr}^{un} = k_{cr}^{anti}(1-\nu_u) = \frac{2\sigma_0(b-a)(1-\nu_u)}{GL} \tag{54}$$

is the critical wavenumber for the corresponding elastic problem of in-plane sliding assuming an undrained Poisson's ratio. We present k_{cr} within an absolute value to reflect that it can be both positive and negative depending on the directionality of the slip wave as was previously discussed. This also implies that, if the right hand side of the equation is negative, then clearly the critical wavenumber does not exist.

Similarly, for drained bulk response

$$\left|k_{cr}\right| \simeq k_{cr}^{d}\left(1 - \frac{f_0\gamma}{\beta\sigma_0(b-a)} + \mathcal{O}(\epsilon)\right), \tag{55}$$

where

$$k_{cr}^{d} = k_{cr}^{anti}(1-\nu) = \frac{2\sigma_0(b-a)(1-\nu)}{GL} \tag{56}$$

is similarly the drained elastic critical wavenumber of in-plane sliding.

For anti-plane sliding, there is no difference in the bulk response at drained or undrained condition (to zeroth order in ϵ') and the corresponding limit is simply

$$\left|k_{cr}\right| \simeq k_{cr}^{anti}\left(1 - \frac{f_0\gamma}{\beta\sigma_0(b-a)} + \mathcal{O}(\epsilon)\right), \tag{57}$$

We thus observe that the dilatancy has a primary effect on the critical wavenumber in this limit. Equations 53 and 57 are, in a sense, equivalent to the undrained limit identified by Segall and Rice (1995) with a single-degree-of-freedom spring-slider analysis, except Equations 53 and 57 are for a deformable poroelastic bulk. However, Equation 55 does not have a direct correspondence in the Segall and Rice (1995) analysis. This is because the Segall and Rice (1995) analysis had effectively only one diffusion time controlled by the hydraulic diffusivity c of the bulk. Here, we consider that the time scale of flux within the shear layer may be very different (see Section 4.1). Thus this analysis adds to the findings of Segall and Rice (1995) by suggesting that, as long as the shear layer is sufficiently impermeable, then dilatancy stabilization can occur even in a highly diffusive surroundings.

The first-order correction for Equations 53 and 55 can be written out explicitly as:

$$\mathcal{O}(\epsilon) = \epsilon \frac{2 f_0\gamma(f_0\gamma - (b-a)\phi\sigma_0(\beta_f^p + \beta_n^p))(\beta_g^p + \phi(\beta_f^p - \beta_g^p))(\beta_f^p - \beta_f^\sigma + \beta_n^p + \beta_n^\sigma)}{L\phi^2\sigma_0(\beta_f^p + \beta_n^p)^3(b-a)(1-\phi)}. \tag{58}$$

The corresponding anti-plane $\mathcal{O}(\epsilon)$ correction term in Equation 57 is obtained by multiplying the in-plane correction (Equation 58) by $1/(1-\nu)$ and $1/(1-\nu_u)$ for the drained and undrained bulk responses, respectively.

This correction arises due to the shear-zone expansion from non-elastic porosity changes from dilatancy and elastic porosity changes due to pore pressure change and normal stress changes. It is likely that the sign of this term is mostly governed by the sign of $f_0\gamma - (b-a)\phi\sigma_0(\beta_f^p + \beta_n^p) = f_0\gamma - (b-a)\sigma_0\beta$. Thus, if $f_0\gamma/((b-a)\sigma_0\beta) > 1$, this term would act to destabilize. However, $f_0\gamma/((b-a)\sigma_0\beta) = 1$ is the condition when Equations 53, 55, and 57 suggest no unstable wavenumbers, since $k_c = 0$ to the leading order. We thus conclude that, for sets of parameters where the interface is conditionally unstable due to small perturbations around steady state, fault-perpendicular displacements act to further stabilize sliding as $\kappa_c \rightarrow 0$.

4.3. Undrained Bulk Response ($c \rightarrow 0$)

In this particular limit, we neglect any diffusion of fluids in the bulk. However, we note that the shearing layer itself can equilibrate pore pressure, in other words, $\kappa_c > 0$. In this particular case, the characteristic equation is greatly simplified because $\bar{H}_1 \rightarrow 1$ and $\bar{H}_2 \rightarrow 1$ by design (Heimisson et al., 2019). However the full solution to the system is still too complicated to provide any useful insight if written out as an equation. We thus approximate the characteristic equation following the procedure outlined before. We obtain the following expression:

$$\left|k_{cr}\right| \simeq k_{cr}^{un} \frac{1}{1+\mathcal{C}}, \tag{59}$$

where $\mathcal{C}$ is a non-dimensional and non-negative parameter:

$$\mathcal{C} = \epsilon \frac{2 f_0\gamma(3 - 2B(1+\nu_u))}{3L(1-\phi)} \tag{60}$$

The corresponding anti-plane limit is obtained by substitution of $k_{cr}^{un} \rightarrow k_{cr}^{anti}$ and $\mathcal{C} \rightarrow \mathcal{C} \,/\, (1-\nu_u)$.

In the limit $\epsilon \rightarrow 0$, we clearly see that $k_{cr} = k_{cr}^{un}$ as is expected. It is notable that $\mathcal{C}$ describes stabilization due to expansion of the gouge in response to inelastic dilatancy, which causes fault perpendicular displacements. The bracket $3 - 2B(1+\nu_u) \geq 0$, since at most $B = 1$ and $\nu_u = 0.5$. This bracket characterizes the competition between two processes: increased compression of the shear layer due to expansion against the poroelastic host rock and increased pore pressure in the shear layer due to the compression of the host rock. If $B = 1$, and the undrained Poisson's ratio of the host rock implies that it is nearly incompressible, the two effects cancel completely. We conclude that the influence of the shear layer expansion in the undrained bulk limit can be neglected as long as

$$\mathcal{C} = \epsilon \frac{2 f_0\gamma(3 - 2B(1+\nu_u))}{3L(1-\phi)} \ll 1. \tag{61}$$

It is worth noting that higher order terms may become significant in the limit of $\kappa_c \rightarrow 0$. But, as we recognized in the previous section, the limit of $\kappa_c = 0$ gives rise to dilatancy stabilization of the zeroth order with respect to ϵ. By retaining the leading-order terms with dependence on $1/\kappa_c$, we find that, in order for Equation 60 to be a valid approximation, one needs to have:

$$\epsilon^4 \frac{V_0^2 \beta f_0 \gamma}{4L^2 \kappa_c^2 a \sigma_0} \ll 1. \tag{62}$$

If the inequality is violated, we expect the onset of stabilization through dilatancy in the sense identified by Segall and Rice (1995).

4.4. Drained Bulk Response ($c \to \infty$)

In this limit, we assume that the bulk is highly diffusive on any time scale relevant to dilatancy and for the onset of instability. However, we assume that the shear layer pressure equilibrates on a finite time scale, that is, $\kappa_c > 0$. We carry out the same procedure as for undrained bulk response to obtain an approximate expression for the critical wavenumber:

$$\left|k_{cr}\right| \simeq k_{cr}^{d} \frac{1}{1 + \mathcal{C}_d}. \tag{63}$$

Curiously, this approximation has exactly the same form as for the undrained bulk with some slight changes:

$$k_{cr}^{d} = \frac{2\sigma_0 (b - a)(1 - \nu)}{GL} \tag{64}$$

and

$$\mathcal{C}_d = \epsilon \frac{2 f_0 \gamma}{L(1 - \phi)}. \tag{65}$$

The corresponding anti-plane limit is obtained by substitution of $k_{cr}^{d} \to k_{cr}^{anti}$ and $\mathcal{C}_d \to \mathcal{C}_d\, /\, (1 - \nu)$.

The critical wavenumber for the undrained bulk response (Equation 59) can be turned into the one for the drained bulk response (Equation 63) simply by substituting $\nu_u \to \nu$ and setting $B = 0$. The substitution of the undrained Poisson's ratio by the drained one is obviously relevant. The substitution of $B = 0$ is also easily explained since, for the fully drained bulk response, fault perpendicular movements do not induce an increased pore pressure adjacent to the shear zone.

It is worth noting that the only compressibility that shows up in Equations 59 and 63 is $\beta = \phi(\beta_f^p + \beta_n^p)$ (defined in the same way as by (Segall & Rice, 1995)). All other compressibilities, such as those related to uniaxial compression or the fault gouge compressibilities, influence the solution through higher-order terms that are neglected here, which indicates that the other compressibilities are not as important.

In the drained bulk limit, a violation of inequality (Equation 62) also indicates the onset of traditional dilatancy stabilization as in Segall and Rice (1995).

5. Results

In the results section we solve the characteristic equation using a standard root-finding algorithm. We focus on two parameter regimes for bulk and poroelastic properties: a Westerly Granite with $B = 0.81$, $\nu = 0.25$, $\nu_u = 0.33$ and an Ohio sandstone with $B = 0.50$, $\nu = 0.18$, and $\nu_u = 0.28$, both under in-plane and anti-plane sliding. We selected Westerly Granites since it is commonly used in various rock mechanics experiments. The Ohio Sandstone values where then picked to give an example of a material with significantly different poroelastic constants. These values are taken from the poroelastic material parameters for rocks listed in Cheng (2016) (see also references therein).

In addition to exploring the granite and sandstone, we also explore two limits - a thinner shear layer with $\epsilon = 1$ mm and a thicker shear layer with $\epsilon = 10$ cm – which would reveal differences corresponding to the fault-normal displacement stabilization process. Other chosen parameters are listed in Appendix (Table A1).

5.1. In-Plane Shear

We first investigate the case of in-plane sliding which gives rise to more variability in the drained and undrained limits and better highlights the different regimes previously discussed.

Figure 2 illustrates how varying the non-dimensional flux time scale $\mathcal{T}_f$ while fixing the non-dimensional bulk-diffusion time scale $\mathcal{T}_b$ alters the critical wavenumber. Generally, a low flux time scale, for example, due to low permeability of the shear zone, translates into more stabilized slip since dilatancy of the shear zone can increase the effective normal stress and increase the frictional resistance. However, this effect is not only controlled by the time scale of shear-zone flux, because a more diffusive bulk will limit the range at which dilatancy can stabilize sliding. However, in the extreme limit that the bulk diffusion is very fast, but shear zone flux is very small, dilatancy can still stabilize. See, for example, the bright yellow line in Figure 2 or dark blue line in Figure 3. However, this limit is less stable than when both $\mathcal{T}_f$ and $\mathcal{T}_b$ are small, since the bulk response is drained and thus has effectively a lower Poisson's ratio.

We clearly observe that the analytical estimates of Section 4.2 derived for the limit of $\kappa_c = 0$ for drained and undrained bulk response generally hold in all cases when solving the complete characteristic equation (Figures 2 and 3, black solid and dashed lines). Similarly we see good agreement in the case of a thicker shear zone (panels b and d) where the critical wavenumber is further reduced as a consequence of fault-normal displacements. In the limit of drained bulk response and high flux (gray solid line) there is significantly stabilization compared to the thinner shear zone, but the first-order correction shows some mismatch in these cases (panels b and d in Figures 2 and 3), indicating that higher-order terms are becoming important, as would be expected for a wider shear layer. We observe that the curious limit of high-flux but undrained bulk response (gray dashed line) is not an actual limiting case, but rather describes an intermediate stability characteristic in a certain parameter range for the thinner shear layer (panels a and c). This is not surprising, since the two time scales, $\mathcal{T}_f$ and $\mathcal{T}_b$, are not independent, in the sense that the flux time scale also depends on the hydraulic diffusivity of the bulk. Thus a limit where the bulk can be considered undrained but the flux time scale is fast can only approximately hold over a certain range of time scales. This intermediate stability characteristics of high-flux but undrained bulk response (gray dashed line) shows up quite clearly in the cases of a thinner shear zone (Figures 2 and 3a,c and c) as clustering or bending of the plotted lines.

For the thicker shear layer (Figures 2 and 3, panels b and d), we find substantial stabilization in comparison with the thinner shear layer especially in the limit of high flux and high bulk diffusivity (gray solid lines), which occurs due to the fault-normal displacements from dilatancy and the associated increase in normal stress on the shearing layer. Since this effect occurs even in the drained limit, it would also be predicted if the bulk were modeled as simple elastic material.

It is notable that under in-plane sliding the lowest possible critical wavenumber, representing the highest degree of stability at steady state, is not in limit where $\mathcal{T}_f$ and $\mathcal{T}_b$ are both small, which is the completely undrained limit. It can be seen clearly in Figure 3, that at near $\mathcal{T}_b \sim 1$ certain lines have a dimple going below black dashed line. Since this occurs $\mathcal{T}_b \sim 1$ and, as we will see in the following subsection, does not occur for the anti-plane sliding, we conclude that this additional stabilization occurs due to a transient poroelastic response of the bulk.

5.2. Anti-Plane Sliding

Here we explore the stability of the steady state for anti-plane sliding. Since Equation 19 has no dependence on Poisson'|'s ratio and no transient poroelastic response, we observe much less variability in stability in the explored limiting cases than for the in-plane sliding.

Figures 4 and 5 illustrate that, as expected, the anti-plane case is much simpler than the in-plane one. This is because dilatancy induced pore-pressure changes are dominating the stability characteristic, but the drained and undrained bulk response in the anti-plane case is less significant and arises only from the dif-

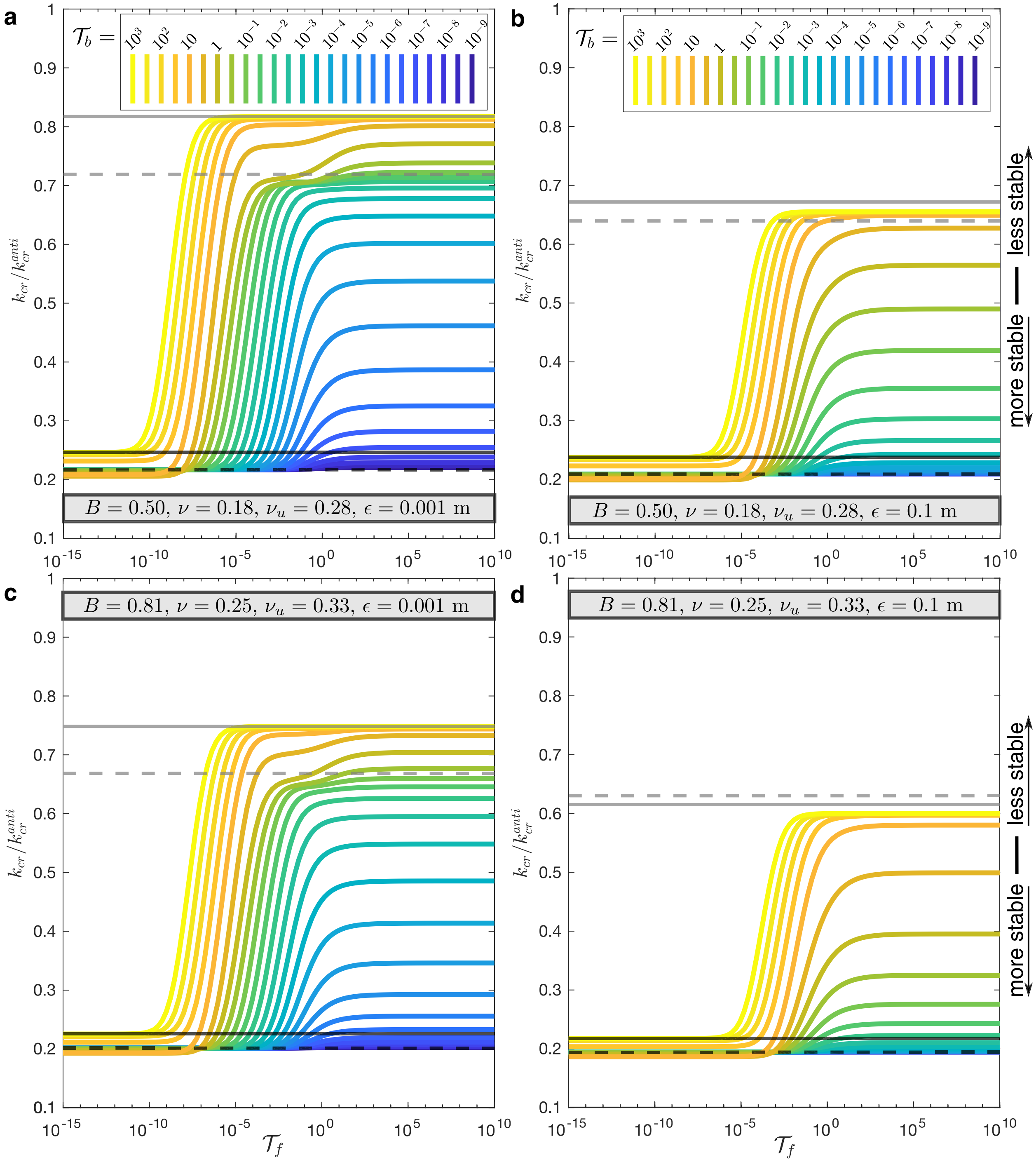

Figure 2. Changes in critical wavenumber k_{cr}, non-dimensionalized by k_{cr}^{anti}, when varying $\mathcal{T}_f$ and keeping $\mathcal{T}_b$ fixed at various values, for in-plane shear. The limit of the undrained bulk and $\kappa_c = 0$ (Equation 53) is shown by black dashed line. The limit of the drained bulk and $\kappa_c = 0$ (Equation 55) is shown by the black solid line. The dashed and solid gray lines indicate the results for the undrained and drained bulk, respectively, with the leading-order ϵ correction (Equations 59 and 63). (a**)** Ohio Sandstone and thinner shear zone. (b**)** Ohio Sandstone and thicker shear zone. (c) Westerly Granite and thinner shear zone. (d) Westerly Granite and thicker shear zone. We generally observe that the numerical solution coincides with the relevant analytical estimates obtained, although, the estimate for the undrained bulk with the leading order ϵ correction only works well for the thinner shear zones.

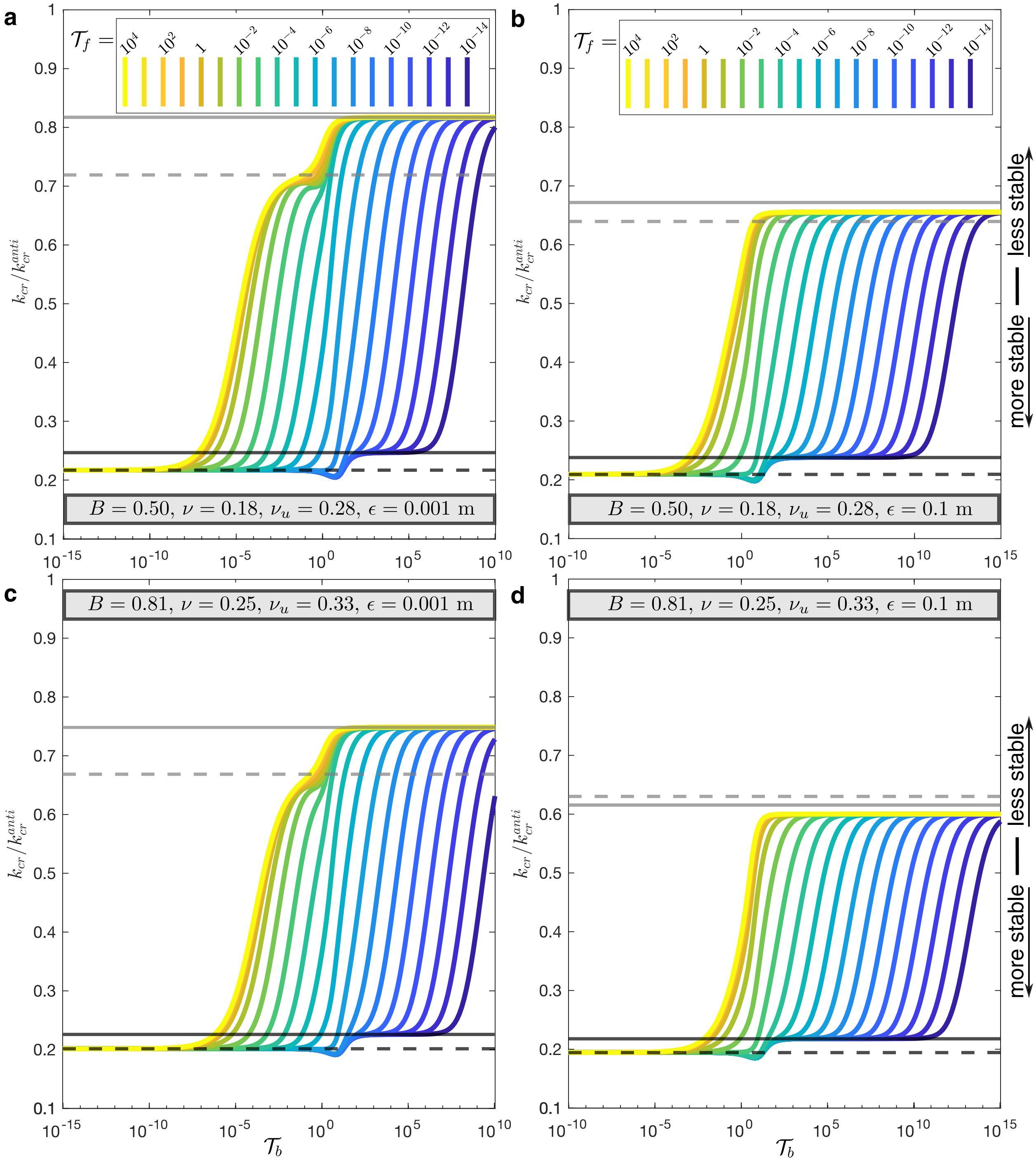

Figure 3. Changes in critical wavenumber k_{cr}, non-dimensionalized by k_{cr}^{anti}, when varying $\mathcal{T}_b$ but keeping $\mathcal{T}_f$ fixed, for in-plane shear. Definitions of lines and panels are the same as in Figure 2.

ferences in effective normal stress (Equations 20 and 21), but not through the sliding-induced shear stress changes (Equation 19). However, these differences in drained and undrained bulk response are very small as can be seen by how the solid and dashed lines in Figures 4 and 5 (a and d) appear to be overlapping. This highlights that poroelasticity can play an important role through shear stress changes during rupture propagation or event nucleation, but only for in-plane sliding.

10.1029/2021JB022071

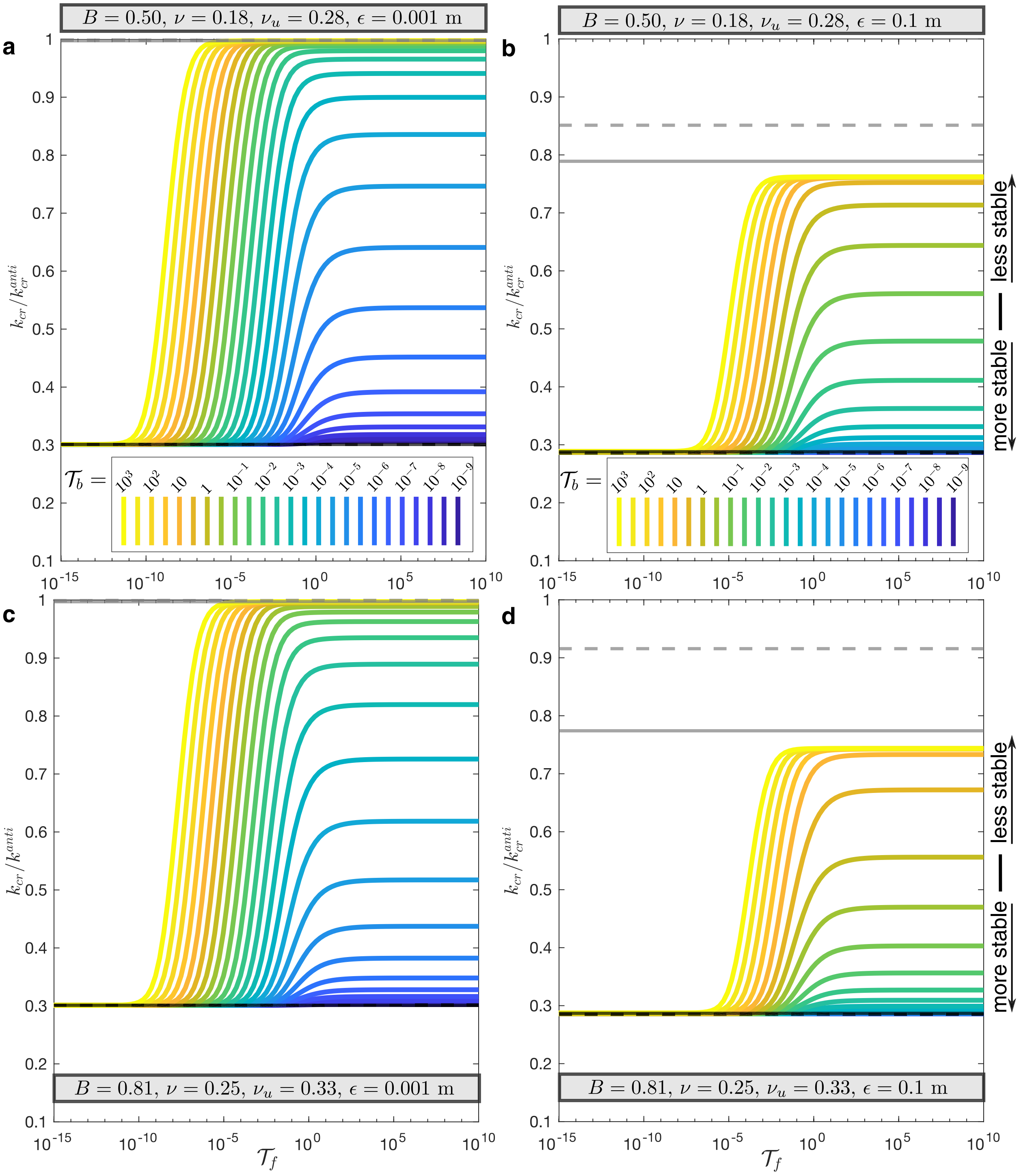

Figure 4. Changes in critical wavenumber k_{cr}, non-dimensionalized by k_{cr}^{anti}, when varying $\mathcal{T}_f$ but keeping $\mathcal{T}_b$ fixed, for anti-plane sliding. The black dashed line indicates an estimate of the critical wavenumber for the limit of the undrained bulk and $\kappa_c = 0$. Black solid line represents the critical wavenumber for drained bulk and $\kappa_c = 0$ limit (Equation 57). Gray dashed line represents results for the undrained bulk with leading order ϵ correction (see Equation 59 and following text). Solid gray line is the drained bulk with leading order ϵ correction (see Equation 63 and following text). (a) Ohio Sandstone and thinner shear zone. (b) Ohio Sandstone and thicker shear zone. (c) Westerly Granite and thinner shear zone. (d) Westerly Granite and thicker shear zone.

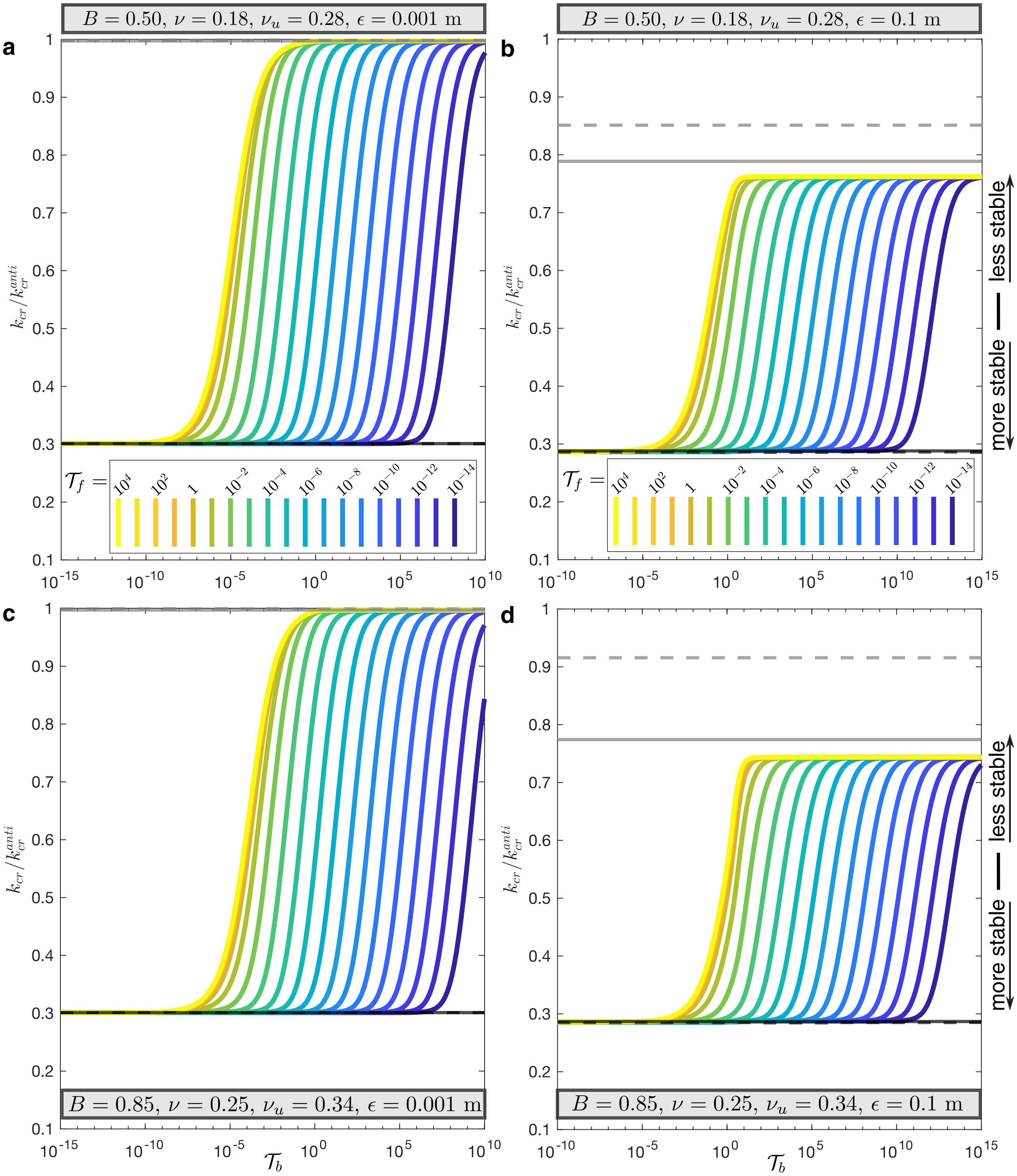

Figure 5. Changes in critical wavenumber k_{cr}, non-dimensionalized by k_{cr}^{anti}, when varying $\mathcal{T}_b$ but keeping $\mathcal{T}_f$ fixed, for anti-plane sliding. Definitions of lines and panels are the same as in Figure 4.

In general, all the same limits exist as for the in-plane case, except we do not observe the intermediate stability characteristic for the undrained bulk with high flux (gray dashed line), furthermore, we do not observe the increased stability beyond the fully undrained limit around near $\mathcal{T}_b \sim 1$ (e.g., Figure 3). However, many similarities remain, for example, we see that that in the anti-plane case, much like the in-plane case, dilatancy induced pore-pressure changes are possible even if the bulk is highly diffusive, as long as the shear zone flux is sufficiently low. Further, we see that stability is for anti-plane is also characterized by the competition of time-scales: $\mathcal{T}_b$ and $\mathcal{T}_f$, where if one is large the stability can still be changed dramatically by making the other sufficiently small. The presence of this competition or interaction of time scales, in both in-plane and anti-plane sliding, suggests that problems involving fluid interactions with frictional sliding may be lacking important insights if they are simplified to a problem with a single diffusion time. Further, it stands to reason that if the problem has more diffusional timescales than $\mathcal{T}_b$ and $\mathcal{T}_f$ the stability may be altered in unexpected ways.

6. Discussion

6.1. Comparison With Segall and Rice (1995)

This study is greatly influenced by the seminal work of Segall and Rice (1995), which showed that inelastic dilatancy can significantly stabilize sliding of a frictional interface. This theory has received particular notice since it offers a physical explanation for generating slow slip events on faults (Segall et al., 2010). It is, therefore, worth summarizing and highlighting some of the differences between the analysis presented here and the original analysis of Segall and Rice (1995).

The most fundamental difference between the stability analysis in Segall and Rice (1995) and in our study is the treatment of the bulk. We present the stability analysis in a fully coupled poroelastic medium, whereas Segall and Rice (1995) used a single-degree-of-freedom spring-slider representation of the bulk. Thus, instead of solving for a critical wavenumber (or wavelength) of a perturbation, they solved for the critical spring stiffness. Using elementary fracture mechanics for crack stiffness, one can interpret the spring-slider analysis in terms of the critical wavenumber (e.g., Dieterich, 1992). Indeed, our equation (57), for example, provides results completely consistent with the spring-slider analysis up to a scaling factor of order 1 and ignoring the $O(\epsilon)$ correction. However, other aspects of the stability determined in this study cannot be captured with the spring-slider analysis; for example, the transient stability regimes where neither drained nor undrained response dominates (Figures 2–5). Such regimes depend on the wavenumber (Equation 49), which changes one of the relevant diffusion times, and thus cannot be captured by rescaling of the critical stiffness (e.g., Equations 16 and 17). In Segall and Rice (1995), the transient stability regimes, controlled by a relevant diffusion time, do not depend on a length scale.

The second key difference is the presence of two time scales at which pressure equilibration occurs. These are the time scale of pressure equilibration through shear layer flux $\mathcal{T}_f$, and the time scale related to the diffusion through the bulk $\mathcal{T}_b$. Segall and Rice (1995) and the alternative diffusion model in Segall et al. (2010) only have one diffusion time scale. The analysis with two diffusion time scales provides additional insights into the problem. For example, there is a parameter range where the bulk diffusion can be extremely fast and the bulk response can be considered drained. However, the shear-layer flux time scale is sufficiently slow such that dilatancy can act to stabilize sliding by reducing pore pressure and increasing effective normal stress. That limit may be of important geological relevance. It has been frequently reported that the fault core, where shear localization occurs, has very low permeability (Behnsen & Faulkner, 2011; Caine et al., 1996; Wibberley & Shimamoto, 2003), while the adjacent damage zone is highly permeable (F. Chester & Logan, 1986; Mitchell & Faulkner, 2012).

The final key difference, which is also discussed in some detail in the following subsection, is that our study accounts for the fault-normal displacements that arise from dilatancy and pressure changes in the shear zone. This effect was not considered by Segall and Rice (1995), and it has not been studied previously in the fault mechanics literature to the best of our knowledge. As has been shown here, this effect gives rise to a different mechanism through which dilatancy can stabilize sliding.

6.2. Fault-Normal Displacements

Theoretical studies and field-based observations usually support the idea that seismic slip in fault gouge occurs in an extremely localized shear layer of 1–100 μm. The stability analysis and numerical simulations of Rice et al. (2014) and Platt et al. (2014) used a thermo-poro-mechanical model and suggested that the width of a shear zone arises as a competition between destabilizing thermal pressurization process and a stabilizing process that may be dilatancy or rate-strengthening friction. In the absence of a stabilizing process, the shear zone thickness becomes infinitesimal. Their findings are generally supported in field observations. For example, J. S. Chester et al. (2005) examined the shear zone of the Punchbowl fault in California which has been exhumed from 2–4 km depths and found the principal shear layer of 100–300 microns. De Paola et al. (2008) examined cataclastic fault cores in the Northern Apennines and observed extreme shear strain localization of some tens of microns. However, studies also suggest that the shear layer can be wider. Boullier et al. (2009) examined two borehole cores, which intersected the Chelungpu fault at about 1 km depth after the Chi-Chi earthquake in 1999. Their analysis suggested thin shear localization zone from one core of 2 mm and the other 20 mm. While these widths are small compared to virtually all other characteristic dimensions of that earthquake, it does suggest that even localization at seismic ruptures can vary substantially.

In this study, we have focused on the stability around steady-state quasi-static (slow) sliding. It is less clear how localized the shear zones are at creep rates in the range of centimeters to millimeters per year. Laboratory experiments suggest that the width of such localization depends on the normal stress, where a more delocalized shear-zone is formed at low normal stress (Torabi et al., 2007). These observations beg the question of how localized are the shear zones in regions of slow slip and tectonic tremor in subduction zones. The same question applies to the roots of some strike-slip faults where it has been suggested that pore pressure may be near lithostatic (e.g., Rubinstein et al., 2007; Thomas et al., 2009). It has recently been argued that tectonic mélanges, some hundreds of meters thick, may play an important role in aseismic slip processes along the subduction zone interface (Fagereng et al., 2018; Raimbourg et al., 2019). It is not clear if such large structures can be regarded as a single shear zone and would thus fall under the scope of our analysis. However, geological observations of mélanges strongly suggest that not all shear strain on faults occurs in extremely localized zones.

If the shear layers are sufficiently thick during quasi-static shear, as appears to be possible from lab and field observations, then they can generate fault-normal displacements that stabilize sliding. These displacements are largely caused by the same dilatancy process that reduces pore pressure in the shear zone. The additional stabilization due to fault-normal displacements occurs because the shear layer must expand against the stiff host rock, where slip speed is increasing, and that increases the normal stress on the layer and hence its resistance to sliding. Similarly, where slip speed decreases, the shear zone compacts which reduces normal stress and resistance to sliding. This may also stabilize sliding since the reduced normal stress causes the perturbation in slip speed to decrease and tend to steady state and the reduced normal stress may prevent a local increase in shear stress on the fault. decreases From Equations 63 and 65, we can infer that if $\mathcal{C}_d = \epsilon 2 f_0 \gamma \,/\, L(1-\phi)$ is order 1/10 then shear-zone expansion, in drained conditions, will produce significant stabilization due to shear-zone expansion. Since $2f_0/(1-\phi)$ is typically order 1, we suggest that the shear zone thickness produces significant stabilizing fault-normal displacements through dilatancy if $\epsilon \gtrsim 0.1\, L/\gamma$. Taking $L \sim 10\ \mu$m and $\gamma \sim 10^{-4}$ indicates that the shear layer of the width $\epsilon \sim 1$ cm can be considered an approximate threshold at which fault-normal displacements are large enough to produce a significant stabilizing effect. The same estimate is found for drained bulk (see Equation 61) if $(3-2B(1+\nu_u)) \sim 1$, which is typically true.

We hypothesize that, during shear localization, the fault-normal motion may delay or perhaps prevent further localization, since a perturbation, which otherwise could induce an instability process with extreme localization, may be stabilized by the (larger) shear-zone width at that time. Note that the conclusions may be different for other assumptions of the relevant pore pressure values within the fault zone, such as taking the largest value of pore fluid pressure, which would promote localization. Other factors not considered in this study may affect shear localization, such as thermal pressurization of pore fluids considered in Rice et al. (2014) and Platt et al. (2014). However, since the effects of thermal pressurization on the nucleation process is not likely until late in the nucleation process (Segall & Rice, 2006), which is also when inertial effects are important and our analysis would not be valid.

7. Conclusions

The stabilizing effect of dilatancy on slip along a frictional fault has garnered interest since the mechanism was proposed and formulated by Segall and Rice (1995) within the scope of the rate-and-state friction framework. While a number of studies have implemented dilatancy in simulations of slow and fast slip on faults with rate-and-state friction, the implementation and formulation of dilatancy in a fully-coupled poroelastic solid has been missing. Here we present a closed system of equation describing a shearing gouge layer under in-plane and anti-plane loading with rate-and-state dependent friction and undergoing state-dependent dilatancy/compaction.

We have presented a linearized analysis of the stability of shearing in the layer around steady state. We have identified two mechanisms through which dilatancy can stabilize frictional sliding: first, by reducing pore pressure in the shearing layer and second, by expanding the layer and generating fault-normal displacements in the bulk. The former mechanism was identified by Segall and Rice (1995), where they show that it is most effective for an undrained bulk with loss of stabilization as the bulk response approaches the drained limit. We add to this criterion by highlighting that such stabilization can occur even if the bulk is highly diffusive and responds in a drained manner, due to lower flux within the shear layer. The latter mechanism, due to fault-normal displacements, has not been identified previously, to the best of our knowledge. It primarily results from dilatancy-induced expansion of the shear zone. The expanding shear zone presses against the host rock and increases normal stress acting on the shear zone, thus increasing frictional resistance. This effect does not require the presence of pore pressure changes and occurs even if the shear zone and bulk responses are drained.

The results of this study highlight the importance of considering the realistic hydro-mechanical structure of faults around the thin shear layers, including the actual width of the shearing layer as well as the potential difference between the hydraulic diffusivity of the shear layer (which is thin but finite) and the surrounding host rock. The identified stability properties near steady-state sliding will inform future numerical explorations of the full non-linear problem of a shear fault sliding with dilatancy/compaction in a poroelastic solid.

Appendix A: Parameter Values

Here we discuss the parameters that are kept constant when we numerically solve for the roots of the characteristic equations at critical stability, as shown in Figures 2–5. These parameters and their values are summarized in Table A1.

The material parameters that are fixed are the shear modulus G of the bulk, various compressibilities of the gouge, and the reference porosity of the gouge at steady state sliding ϕ_0, which is assumed to be equivalent to the reference void volume per unit volume. We use $G = 30$ GPa which is selected somewhat arbitrarily but which is a common value used for crustal rocks and should be applicable to well-packed fault gouge. The other bulk poroelastic parameters are varied and explained in the main text. It is worth noting that, to explore different values of the non-dimensional parameter $\mathcal{T}_f$ in Figures 2–5 we only change κ_c but, to explore different values of $\mathcal{T}_b$, we change both the hydraulic diffusivity of the bulk and κ_c so that $\mathcal{T}_f$ is fixed (since it depends on both c and κ_c), in accordance with Equations 52 and 51.

In selecting the various gouge material properties, we broadly follow Segall and Rice (1995), Rice et al. (2014), and Platt et al. (2014) where appropriate. We take $\beta_f^p = 0.44 \cdot 10^{-9}$ Pa^{-1} (Fine & Millero, 1973). We use $\beta_n^p = 6.0 \cdot 10^{-9}$ Pa^{-1} which Rice et al. (2014) and Platt et al. (2014) inferred to be appropriate for damaged rocks based on the data by Wibberley and Shimamoto (2003) and using the analysis of Rice (2006). The compressibility of the gouge grains, β_g^p, has not, to the best of our knowledge, been featured in previous literature. We expect this compressibility to be low compared to the fluid or pore compressibilities. We simply assume that it is the inverse of a typical rock bulk modulus of 50 GPa, that is, $\beta_g^p = 0.02 \cdot 10^{-9}$ Pa^{-1}. The uniaxial compressibilities β_f^σ, β_n^σ, and β_g^σ have not received much attention in the previous literature. Here we assume that we can obtain the uniaxial compressibility by multiplying the isotropic compressibility by a factor of 5/9. As discussed in the main text, this is only strictly true for a linear elastic material. However, this likely offers a reasonable correspondence between isotropic and uniaxial compressibility more generally. Nevertheless, we suggest that more studies are needed to determine if uniaxial compressibilities can be vastly different from the isotropic compressibilities. We select the reference porosity at steady-state sliding, also interpreted as the void volume per unit volume, as $\phi = 0.068$. This is a commonly used value based on Wibberley and Shimamoto (2003). Finally, we follow Segall and Rice (1995) in their modeling of the Marone et al. (1990) experiments and select the dilatancy coefficient as $\gamma = 1.7 \cdot 10^{-4}$.

Table A1
Parameters That are Kept Constant in the Study

Symbol	Description	Value
Bulk and gouge material properties		
G	Shear modulus	30 GPa
$\beta_f^p, \beta_f^\sigma$	Isotropic and uniaxial fluid compressibility	$0.44 \cdot 10^{-9}$ Pa^{-1}, $0.24 \cdot 10^{-9}$ Pa^{-1},
$\beta_n^p, \beta_n^\sigma$	Isotropic and uniaxial pore volume compressibility	$6.0 \cdot 10^{-9}$ Pa^{-1}, $3.3 \cdot 10^{-9}$ Pa^{-1},
$\beta_g^p, \beta_g^\sigma$	Isotropic and uniaxial solid gouge compressibility	$0.020 \cdot 10^{-9}$ Pa^{-1}, $0.011 \cdot 10^{-9}$ Pa^{-1},
ϕ_0	Reference porosity	0.068
Friction and loading parameters		
L	Characteristic state evolution distance	100 μm
A	Direct rate dependence of friction	0.01
B	State dependence of friction	0.02
α_{LD}	Linker and Dieterich (1992) constant	0.0
V_0	Steady-state and reference sliding velocity	10^{-9} m s^{-1}
f_0	Steady-state coefficient of friction at V_0	0.6
τ_0	Initial shear stress	20.0 MPa
σ_0	Initial effective normal stress	33.3 MPa

For the friction and fault loading parameters, we select fairly standard values (Table A1) frequently used in the literature. It is worth mentioning that, for simplicity, we have taken the Linker and Dieterich (1992) constant $\alpha_{LD} = 0$, which implies no explicit dependence of the state variable on normal stress changes. This essentially means that we consider the effective normal stress changes to be gradual enough that the shear stress stays proportional to the effective normal stress, a reasonable assumptions given the slow slip considered. In Table A1, we provide both initial shear and normal stress for convenience, but the two are not independent due to the condition that the fault is initially at steady state and are related through $\tau_0 = f_0\sigma_0$.

Throughout the main text, we have mostly used G, B, ν, ν_u, c to fully describe the poroelastic bulk properties. However, in a few cases, we have used different set of parameter for compactness, that is, M, α, and κ. Here we list a few relationships that would allow the reader to convert between these parameter sets:

$$B = \frac{3M\alpha(1-2\nu)}{2G(1+\nu) + 3M\alpha^2(1-2\nu)}$$

$$\nu_u = \frac{2G\nu + M\alpha^2(1-2\nu)}{2G + 2M\alpha^2(1-2\nu)}$$

$$B = \frac{3(\nu_u - \nu)}{\alpha(1-2\nu)(1+\nu_u)}$$

$$c = M\kappa.$$

Data Availability Statement

This is a theoretical paper and contains no data. Code for determining the critical stability and solving Equation 41, which also contains explicit expressions for equations too long to write out in this paper, is found here https://doi.org/10.5281/zenodo.5005276 (see Heimisson, 2021).

Acknowledgments

This study was supported by the Geophysics Option Postdoctoral Fellowship from the Division of Geological and Planetary Sciences at Caltech to E.R.H. and by the NSF-IUCRC Center for Geomechanics and Mitigation of Geohazards (projects GMG-4.1, GMG-4.2) to N.L. We thank reviewers Allan Rubin and Massimo Cocco for their constructive remarks and we thank Paul Segall for helpful comments.

References

Behnsen, J., & Faulkner, D. (2011). Water and argon permeability of phyllosilicate powders under medium to high pressure. *Earth and Planetary Science Letters*, *116*(B12).

Bhattacharya, P., & Viesca, R. C. (2019). Fluid-induced aseismic fault slip outpaces pore-fluid migration. *Science*, *364*(6439), 464–468. https://doi.org/10.1126/science.aaw7354

Bizzarri, A., & Cocco, M. (2006). A thermal pressurization model for the spontaneous dynamic rupture propagation on a three-dimensional fault: 1. Methodological approach. *Journal of Geophysical Research: Solid Earth*, *111*(B5). https://doi.org/10.1029/2005JB003862

Boullier, A.-M., Yeh, E.-C., Boutareaud, S., Song, S.-R., & Tsai, C.-H. (2009). Microscale anatomy of the 1999 chi-chi earthquake fault zone. *Geochemistry, Geophysics, Geosystems*, *10*(3). https://doi.org/10.1029/2008GC002252

Brace, W. F., Paulding, B. W., Jr, & Scholz, C. (1966). Dilatancy in the fracture of crystalline rocks. *Journal of Geophysical Research*, *71*(16), 3939–3953. https://doi.org/10.1029/JZ071i016p03939

Bürgmann, R. (2018). The geophysics, geology and mechanics of slow fault slip. *Earth and Planetary Science Letters*, *495*, 112–134.

Caine, J. S., Evans, J. P., & Forster, C. B. (1996). Fault zone architecture and permeability structure. *Geology*, *24*(11), 1025–1028.

Cheng, A. H.-D. (2016). Poroelasticity (Vol. 877). Springer.

Chester, F., & Logan, J. M. (1986). Implications for mechanical properties of brittle faults from observations of the punchbowl fault zone, California. *Pure and Applied Geophysics*, *124*(1–2), 79–106.

Chester, F. M., Chester, J. S., Kirschner, D. L., Schulz, S. E., & Evans, J. P. (2004). Structure of large-displacement, strike-slip fault zones in the brittle continental crust. *Rheology and deformation in the lithosphere at continental margins*, *1*, 223–260.

Chester, F. M., Evans, J. P., & Biegel, R. L. (1993). Internal structure and weakening mechanisms of the San Andreas fault. *Journal of Geophysical Research*, *98*(B1), 771–786.

Chester, J. S., Chester, F. M., & Kronenberg, A. K. (2005). Fracture surface energy of the punchbowl fault, San Andreas system. *Nature*, *437*(7055), 133–136.

Ciardo, F., & Lecampion, B. (2019). Effect of dilatancy on the transition from aseismic to seismic slip due to fluid injection in a fault. *Journal of Geophysical Research: Solid Earth*, *124*(4), 3724–3743. https://doi.org/10.1029/2018JB016636

Cocco, M., & Rice, J. R. (2002). Pore pressure and poroelasticity effects in Coulomb stress analysis of earthquake interactions. *Journal of Geophysical Research: Solid Earth*, *107*(B2), ESE2-1–ESE2-17. https://doi.org/10.1029/2000JB000138

Dal Zilio, L., Lapusta, N., & Avouac, J.-P. (2020). Unraveling scaling properties of slow-slip events. *Geophysical Research Letters*, *47*(10). https://doi.org/10.1029/2020GL087477

De Paola, N., Collettini, C., Faulkner, D. R., & Trippetta, F. (2008). Fault zone architecture and deformation processes within evaporitic rocks in the upper crust. *Tectonics*, *27*(4). https://doi.org/10.1029/2007TC002230

Detournay, E., & Cheng, A. H.-D. (1995). Fundamentals of poroelasticity. *Analysis and design methods*, 113–171. Elsevier.

Dieterich, J. H. (1979). Modeling of rock friction: 1. experimental results and constitutive equations. *Journal of Geophysical Research: Solid Earth*, *84*(B5), 2161–2168. https://doi.org/10.1029/JB084iB05p02161

Dieterich, J. H. (1992). Earthquake nucleation on faults with rate-and state-dependent strength. *Tectonophysics*, *211*(1–4), 115–134. https://doi.org/10.1016/0040-1951(92)90055-B

Dor, O., Rockwell, T. K., & Ben-Zion, Y. (2006). Geological observations of damage asymmetry in the structure of the San Jacinto, San Andreas and Punchbowl faults in Southern California: A possible indicator for preferred rupture propagation direction. *Pure and Applied Geophysics*, *163*(2), 301–349. https://doi.org/10.1007/s00024-005-0023-9

Dunham, E. M., & Rice, J. R. (2008). Earthquake slip between dissimilar poroelastic materials. *Journal of Geophysical Research: Solid Earth*, *113*(B9), B09304. https://doi.org/10.1029/2007JB005405

Ellsworth, W. L. (2013). Injection-induced earthquakes. *Science*, *341*(6142), 1225942.

Fagereng, Å., Diener, J. F., Ellis, S., & Remitti, F. (2018). Fluid-related deformation processes at the up-and down-dip limits of the subduction thrust seismogenic zone: What do the rocks tell us. *Geological Society of America Special Paper*, Vol. *534*.

Ferdowsi, B., & Rubin, A. M. (2020). A granular physics-based view of fault friction experiments. *Journal of Geophysical Research: Solid Earth*, *125*(6), e2019JB019016. https://doi.org/10.1029/2019JB019016

Fine, R. A., & Millero, F. J. (1973). Compressibility of water as a function of temperature and pressure. *The Journal of Chemical Physics*, *59*(10), 5529–5536. https://doi.org/10.1063/1.1679903

Heimisson, E. R. (2021). *eliasrh/Poroelastic_linear_stability: Release for publication of Heimisson, Rudnicki, and Lapusta 2021*. Zenodo. https://doi.org/10.5281/zenodo.5005276

Heimisson, E. R., Dunham, E. M., & Almquist, M. (2019). Poroelastic effects destabilize mildly rate-strengthening friction to generate stable slow slip pulses. *Journal of the Mechanics and Physics of Solids*, *130*, 262–279. https://doi.org/10.1016/j.jmps.2019.06.007

Heimisson, E. R., & Segall, P. (2018). Constitutive law for earthquake production based on rate-and-state friction: Dieterich 1994 revisited. *Journal of Geophysical Research: Solid Earth*, *123*(5), 4141–4156. https://doi.org/10.1029/2018JB015656

Hulikal, S., Lapusta, N., & Bhattacharya, K. (2018). Static and sliding contact of rough surfaces: Effect of asperity-scale properties and long-range elastic interactions. *Journal of the Mechanics and Physics of Solids*, *116*, 217–238. https://doi.org/10.1016/j.jmps.2018.03.022

Jha, B., & Juanes, R. (2014). Coupled multiphase flow and poromechanics: A computational model of pore pressure effects on fault slip and earthquake triggering. *Water Resources Research*, *50*(5), 3776–3808. https://doi.org/10.1002/2013WR015175

Jónsson, S., Segall, P., Pedersen, R., & Björnsson, G. (2003). Post-earthquake ground movements correlated to pore-pressure transients. *Nature*, *424*(6945), 179–183. https://doi.org/10.1038/nature01776

Linker, M. F., & Dieterich, J. H. (1992). Effects of variable normal stress on rock friction: Observations and constitutive equations. *Journal of Geophysical Research: Solid Earth*, *97*(B4), 4923–4940. https://doi.org/10.1029/92JB00017

Liu, Y. (2013). Numerical simulations on megathrust rupture stabilized under strong dilatancy strengthening in slow slip region. *Geophysical Research Letters*, *40*(7), 1311–1316. https://doi.org/10.1002/grl.50298

Lockner, D. A., & Byerlee, J. D. (1994). Dilatancy in hydraulically isolated faults and the suppression of instability. *Geophysical Research Letters*, *21*(22), 2353–2356. https://doi.org/10.1029/94GL02366

Lyakhovsky, V., & Ben-Zion, Y. (2020). Isotropic seismic radiation from rock damage and dilatancy. *Geophysical Journal International*, *222*(1), 449–460. https://doi.org/10.1093/gji/ggaa176

Marone, C. (1998). Laboratory-derived friction laws and their application to seismic faulting. *Annual Review of Earth and Planetary Sciences*, *26*(1), 643–696.

Marone, C., Raleigh, C. B., & Scholz, C. H. (1990). Frictional behavior and constitutive modeling of simulated fault gouge. *Journal of Geophysical Research: Solid Earth*, *95*(B5), 7007–7025. https://doi.org/10.1029/JB095iB05p07007

McNamee, J., & Gibson, R. E. (1960). Plane strain and axially symmetric problems of the consolidation of a semi-infinite clay stratum. *Quarterly Journal of Mechanics & Applied Mathematics*, *13*(2), 210–227.

Mitchell, T., & Faulkner, D. (2012). Towards quantifying the matrix permeability of fault damage zones in low porosity rocks. *Earth and Planetary Science Letters*, *339*, 24–31.

Platt, J. D., Rudnicki, J. W., & Rice, J. R. (2014). Stability and localization of rapid shear in fluid-saturated fault gouge: 2. localized zone width and strength evolution. *Journal of Geophysical Research: Solid Earth*, *119*(5), 4334–4359. https://doi.org/10.1002/2013JB010711

Proctor, B., Lockner, D. A., Kilgore, B. D., Mitchell, T. M., & Beeler, N. M. (2020). Direct evidence for fluid pressure, dilatancy, and compaction affecting slip in isolated faults. *Geophysical Research Letters*, *47*(16), e2019GL086767. https://doi.org/10.1029/2019GL086767

Raimbourg, H., Famin, V., Palazzin, G., Yamaguchi, A., Augier, R., Kitamura, Y., & Sakaguchi, A. (2019). Distributed deformation along the subduction plate interface: The role of tectonic mélanges. *Lithos*, *334–335*, 69–87. https://doi.org/10.1016/j.lithos.2019.01.033

Rice, J. R. (2006). Heating and weakening of faults during earthquake slip. *Journal of Geophysical Research: Solid Earth*, *111*(B5). https://doi.org/10.1029/2005JB004006

Rice, J. R., & Cleary, M. P. (1976). Some basic stress diffusion solutions for fluid-saturated elastic porous media with compressible constituents. *Review of Geophysics*, *14*(2), 227–241. https://doi.org/10.1029/RG014i002p00227

Rice, J. R., Lapusta, N., & Ranjith, K. (2001). Rate and state dependent friction and the stability of sliding between elastically deformable solids. *Journal of the Mechanics and Physics of Solids*, *49*(9), 1865–1898.

Rice, J. R., Rudnicki, J. W., & Platt, J. D. (2014). Stability and localization of rapid shear in fluid-saturated fault gouge: 1. linearized stability analysis. *Journal of Geophysical Research: Solid Earth*, *119*(5), 4311–4333. https://doi.org/10.1002/2013JB010710

Rice, J. R., & Ruina, A. (1983). Stability of steady frictional slipping. *Journal of Applied Mechanics*, *50*(2), 343–349.

Rice, J. R., & Simons, D. A. (1976). The stabilization of spreading shear faults by coupled deformation-diffusion effects in fluid-infiltrated porous materials. *Journal of Geophysical Research*, *81*(29), 5322–5334. https://doi.org/10.1029/JB081i029p05322

Rubinstein, J. L., Vidale, J. E., Gomberg, J., Bodin, P., Creager, K. C., & Malone, S. D. (2007). Non-volcanic tremor driven by large transient shear stresses. *Nature*, *448*(7153), 579.

Rudnicki, J. W., & Chen, C.-H. (1988). Stabilization of rapid frictional slip on a weakening fault by dilatant hardening. *Journal of Geophysical Research: Solid Earth*, *93*(B5), 4745–4757. https://doi.org/10.1029/JB093iB05p04745

Rudnicki, J. W., & Koutsibelas, D. A. (1991). Steady propagation of plane strain shear cracks on an impermeable plane in an elastic diffusive solid. *International Journal of Solids and Structures*, *27*(2), 205–225.

Rudnicki, J. W., & Rice, J. R. (2006). Effective normal stress alteration due to pore pressure changes induced by dynamic slip propagation on a plane between dissimilar materials. *Journal of Geophysical Research: Solid Earth*, *111*(B10). https://doi.org/10.1029/2006JB004396

Ruina, A. (1983). Slip instability and state variable friction laws. *Journal of Geophysical Research: Solid Earth*, *88*(B12), 10359–10370. https://doi.org/10.1029/JB088iB12p10359

Segall, P., & Lu, S. (2015). Injection-induced seismicity: Poroelastic and earthquake nucleation effects. *Journal of Geophysical Research: Solid Earth*, *120*(7), 5082–5103.

Segall, P., & Rice, J. R. (1995). Dilatancy, compaction, and slip instability of a fluid-infiltrated fault. *Journal of Geophysical Research: Solid Earth*, *100*(B11), 22155–22171. https://doi.org/10.1029/95JB02403

Segall, P., & Rice, J. R. (2006). Does shear heating of pore fluid contribute to earthquake nucleation? *Journal of Geophysical Research: Solid Earth*, *111*(B9). https://doi.org/10.1029/2005JB004129

Segall, P., Rubin, A. M., Bradley, A. M., & Rice, J. R. (2010). Dilatant strengthening as a mechanism for slow slip events. *J. Geophys. Res. Solid Earth*, *115*(B12).

Song, Y., & Rudnicki, J. W. (2017). Plane-strain shear dislocation on a leaky plane in a poroelastic solid. *Journal of Applied Mechanics*, *84*(2), 021008.

Templeton, E. L., & Rice, J. R. (2008). Off-fault plasticity and earthquake rupture dynamics: 1. dry materials or neglect of fluid pressure changes. *Journal of Geophysical Research: Solid Earth*, *113*(B9). https://doi.org/10.1029/2007JB005529

Thomas, A. M., Nadeau, R. M., & Bürgmann, R. (2009). Tremor-tide correlations and near-lithostatic pore pressure on the deep San Andreas fault. *Nature*, *462*(7276), 1048–1051. https://doi.org/10.1038/nature08654

Torabi, A., Braathen, A., Cuisiat, F., & Fossen, H. (2007). Shear zones in porous sand: Insights from ring-shear experiments and naturally deformed sandstones. *Tectonophysics*, *437*(1), 37–50. https://doi.org/10.1016/j.tecto.2007.02.018

Torberntsson, K., Stiernström, V., Mattsson, K., & Dunham, E. M. (2018). A finite difference method for earthquake sequences in poroelastic solids. *Computational Geosciences*, *22*(5), 1351–1370. https://doi.org/10.1007/s10596-018-9757-1

Verruijt, A. (1971). Displacement functions in the theory of consolidation or in thermoelasticity. *Zeitschrift für angewandte Mathematik und Physik ZAMP*, *22*(5), 891–898.

Viesca, R. C., & Dublanchet, P. (2019). The slow slip of viscous faults. *Journal of Geophysical Research: Solid Earth*, *124*(5), 4959–4983. https://doi.org/10.1029/2018JB016294

Viesca, R. C., Templeton, E. L., & Rice, J. R. (2008). Off-fault plasticity and earthquake rupture dynamics: 2. effects of fluid saturation. *Journal of Geophysical Research: Solid Earth*, *113*(B9). https://doi.org/10.1029/2007JB005530

Wibberley, C. A., & Shimamoto, T. (2003). Internal structure and permeability of major strike-slip fault zones: The Median Tectonic Line in Mie Prefecture, Southwest Japan. *Journal of Structural Geology*, *25*(1), 59–78.